Bulletin of the Seismological Society of America, Vol. 108, No. 1, pp. 1–18, February 2018, doi: 10.1785/0120170159

A Comprehensive Analysis of Geodetic Slip-Rate Estimates and Uncertainties in California

by Eileen L. Evans

Abstract Developing a comprehensive model of tectonic continental deformation requires assessing (1) fault-slip rates, (2) off-fault deformation rates, and (3) realistic uncertainties. Fault-slip rates can be estimated by modeling fault systems, based on space geodetic measurements of active surface ground displacement such as Global Navigation Satellite Systems (GNSS) and Interferometric Synthetic Aperture Radar (InSAR). Geodetic slip-rate estimates may vary widely due to measurement and epistemic (model) uncertainties, presenting a challenge for both estimating slip rates and accurately characterizing uncertainties: models may vary in the number of faults represented and the precise location of those faults. Since 2003, 33 published geodetic deformation models have produced slip-rate estimates within California. Variability among these models represents variability among valid model choices and may be considered a proxy for model uncertainties in geodetic slip-rate estimates. To enable rigorous comparison between geodetic slip-rate estimates, I combine models on a georeferenced grid and find an average standard deviation on slip rate of ∼1.5 mm/yr over 542 grid cells (average area of 1304 km^2/cell). Furthermore, the average strike-slip and tensile-slip rates over all 33 studies, in each grid cell, may then be projected onto Unified California Earthquake Rupture Forecast (UCERF) v.3.1 faults for a single summary model of geodetic slip rates. Slip rates that do not project perfectly onto UCERF3.1 faults form a summary model of off-modeled-fault (OMF) deformation. Most of this OMF deformation occurs in grid cells that intersect UCERF3.1 faults, suggesting that off-fault deformation may be, in part, a product of epistemic uncertainty in geodetic slip-rate estimates and may be physically accommodated on, or very near, UCERF faults.

Electronic Supplement: Figures showing the results of the geodetic slip-rate analysis in California on different geographic grid sizes.

Introduction

Fault-slip rate—the rate at which displacement on a fault occurs on tectonic timescales—is a fundamental parameter in understanding how tectonic strain is distributed across faults in the plate boundary, and a metric that goes directly into earthquake hazard models (e.g., Petersen *et al.*, 2014). Along with earthquake recurrence interval, the rate at which strain accumulates on a fault in the interseismic period of the earthquake cycle is the most important factor contributing to the size and location of the resulting earthquake. Estimates of long-term fault-slip rate can be modeled based on space geodetic measurements of surface ground displacement (Global Navigation Satellite Systems [GNSS] and Interferometric Synthetic Aperture Radar [InSAR]) and a modeled fault surface. Geodetically determined long-term slip rates are expected, in many cases, to be equal to geologic slip rates (e.g., Savage and Burford, 1973; Meade *et al.*, 2013), which are estimated directly at points along mapped faults using tectonic geomorphology.

Most geodetic observations are made during the time between major earthquakes, when seismogenic faults are locked, and geodetic-based fault-slip rates must be estimated within the context of a crustal deformation model in which fault locations and locking depths are prescribed. Because elastic strain accumulation around locked faults produces a smooth gradient in crustal velocities, fault locations may not be readily apparent from geodetic observations alone (e.g., Savage and Simpson, 2013; Evans *et al.*, 2015; Thatcher *et al.*, 2016). Furthermore, fault maps may include faults that are no longer active, and/or omit unknown and blind faults (e.g., Nicol *et al.*, 2016). Although it has been shown that

geodetic observations may be more sensitive to fault potency (or geometric moment: fault-slip rate multiplied by effective locking depth) than to slip rate alone (Johnson *et al.*, 1994; Maurer and Johnson, 2014; Tong *et al.*, 2014), especially where locking depth may vary considerably along fault strike (e.g., Smith-Konter *et al.*, 2011), geodetic model results are reported typically in terms of estimated long-term slip rate.

Geodetic slip-rate models (GSRMs) in California represent a unique opportunity to quantify variability due to many model assumptions, because of the large number of geographically overlapping models, I consider 33 peer-reviewed GSRMs, from 32 publications since 2003 (Fig. 1; Table 1). The simplest models are 2D dislocation models (Savage and Burford, 1973), which represent faults as dislocations in an elastic half-space, with slip rates estimated from geodetic observations along a fault-perpendicular profile (Fialko, 2006; Lindsey and Fialko, 2013). A similar approach (McGill *et al.*, 2015) estimates fault-slip rates along a profile but includes faults striking off of perpendicular to the profile. Rectangular dislocations may be embedded in a 3D elastic volume (Okada, 1985), allowing realistic fault system geometries for modeling a 2D horizontal surface velocity field (Manaker *et al.*, 2003; Argus *et al.*, 2005; Schmidt *et al.*, 2005; Bürgmann *et al.*, 2006; Rolandone *et al.*, 2008; Ryder and Bürgmann, 2008; Murray *et al.*, 2014; Chaussard *et al.*, 2015; Jolivet *et al.*, 2015). Block models, in which the elastic upper crust is divided into microplates bounded by faults, are an extension of dislocation models in which relative microplate rotations determine slip rates on faults (d'Alessio *et al.*, 2005; McCaffrey, 2005; Meade and Hager, 2005; Hammond and Thatcher, 2007; Spinler *et al.*, 2010; Hammond *et al.*, 2011; Loveless and Meade, 2011; Evans *et al.*, 2012, 2015, 2016; Johnson, 2013; Bormann *et al.*, 2016). Block models may be combined with dislocation models by embedding dislocations in the interior of otherwise rigid blocks (Parsons *et al.*, 2013; Zeng and Shen, 2016). Another suite of models correct for viscoelastic transients following large earthquakes that may bias interseismic slip rates above or below their average long-term slip rates (Chuang and Johnson, 2011; Johnson, 2013; Tong *et al.*, 2014). A less common approach estimates fault-slip rates within a finite-element model (Schmalzle *et al.*, 2006; Bird, 2009).

Comprehensive seismic hazard quantification requires an assessment of uncertainty in geodetic fault-slip-rate estimates, and variability among slip-rate results in the above 33 models may be considered a proxy for epistemic uncertainty in geodetic slip-rate estimates in California. However, differences in geodetic data set, fault geometry, and modeling assumptions all lead to differences in estimated slip rate on a given fault or fault system, which may be larger than the 1–5 mm/yr uncertainties reported by any specific study. Epistemic uncertainty —uncertainty due to lack of perfect knowledge of the modeled system—is a common concept in studies of earthquake-related ground-motion studies (e.g., Budnitz *et al.*, 1997; Douglas and Edwards, 2016). Epistemic uncertainty likely contributes to the total uncertainty in geodetic fault-slip-rate estimates as well. Here, I use the terms "epistemic uncertainty" and "model uncertainty" interchangeably.

Model aggregation is an increasingly popular approach for assessing uncertainty in geophysical models. Ground-motion studies often assess epistemic uncertainty by combining models in a decision tree (e.g., Douglas and Edwards, 2016), a practice that has been included in seismic hazard models (e.g., Petersen *et al.*, 2014) and rupture forecasting (e.g., Field *et al.*, 2013). Model aggregation has been used to characterize model-based uncertainty in finite-earthquake rupture models (Mai and Thingbaijam, 2014) and conceptual uncertainty in seismic reflection images (Bond *et al.*, 2007).

To examine published geodetic slip-rate estimates in California and quantify variability among models, I systematically compile published geodetic slip-rate estimates on a georeferenced grid to compare models spatially. Within each grid cell, a number of summary statistics are calculated based on the estimated fault-slip rates from all relevant models in the cell: spatially averaged velocity gradient, geometric moment, and standard deviation among models. This approach enables rigorous comparison of these 33 models with geologic slip rates in a way that takes variability among geodetic slip-rate estimates into account. The resulting integrated deformation model may be projected onto Unified California Earthquake Rupture Forecast (UCERF; Field *et al.*, 2013) faults to produce a single summary model of geodetic slip rates, off-modeled-fault (OMF) deformation, and uncertainties in California.

Slip-Rate Studies

I aggregate long-term slip rates estimated from geodetic observations, and the geometries on which they are modeled. I selected crustal deformation studies in which long-term fault-slip rates are estimated using inverse methods from primarily geodetic observations. Because I seek to evaluate the role of model choices, I do not include the underlying geodetic observations in the compilation. I consider model fault geometries and slip-rate estimates from 33 geodetic slip-rate studies in California, from 32 publications (the geometry of Johnson, 2013, is used twice, as an elastic and a viscoelastic model; Fig. 1). A summary of the models included and their features is provided in Table 1. In 13 models, fault geometry and slip rates are derived from the manuscript and/or its supplementary material (Manaker *et al.*, 2003; Argus *et al.*, 2005; d'Alessio *et al.*, 2005; Johanson and Bürgmann, 2005; McCaffrey, 2005; Schmidt *et al.*, 2005; Bürgmann *et al.*, 2006; Funning *et al.*, 2007; Rolandone *et al.*, 2008; Ryder and Bürgmann, 2008; Bird, 2009; Murray *et al.*, 2014; Chaussard *et al.*, 2015); 17 model geometries were supplied via personal communication (Meade and Hager, 2005; Spinler *et al.*, 2010; Chuang and Johnson, 2011; Hammond *et al.*, 2011; Loveless and Meade, 2011; Evans *et al.*, 2012, 2015, 2016; Johnson, 2013; Lindsey and Fialko, 2013; Parsons *et al.*, 2013; Jolivet *et al.*, 2015; McGill *et al.*, 2015; Bormann *et al.*, 2016; Zeng and Shen, 2016). Two studies

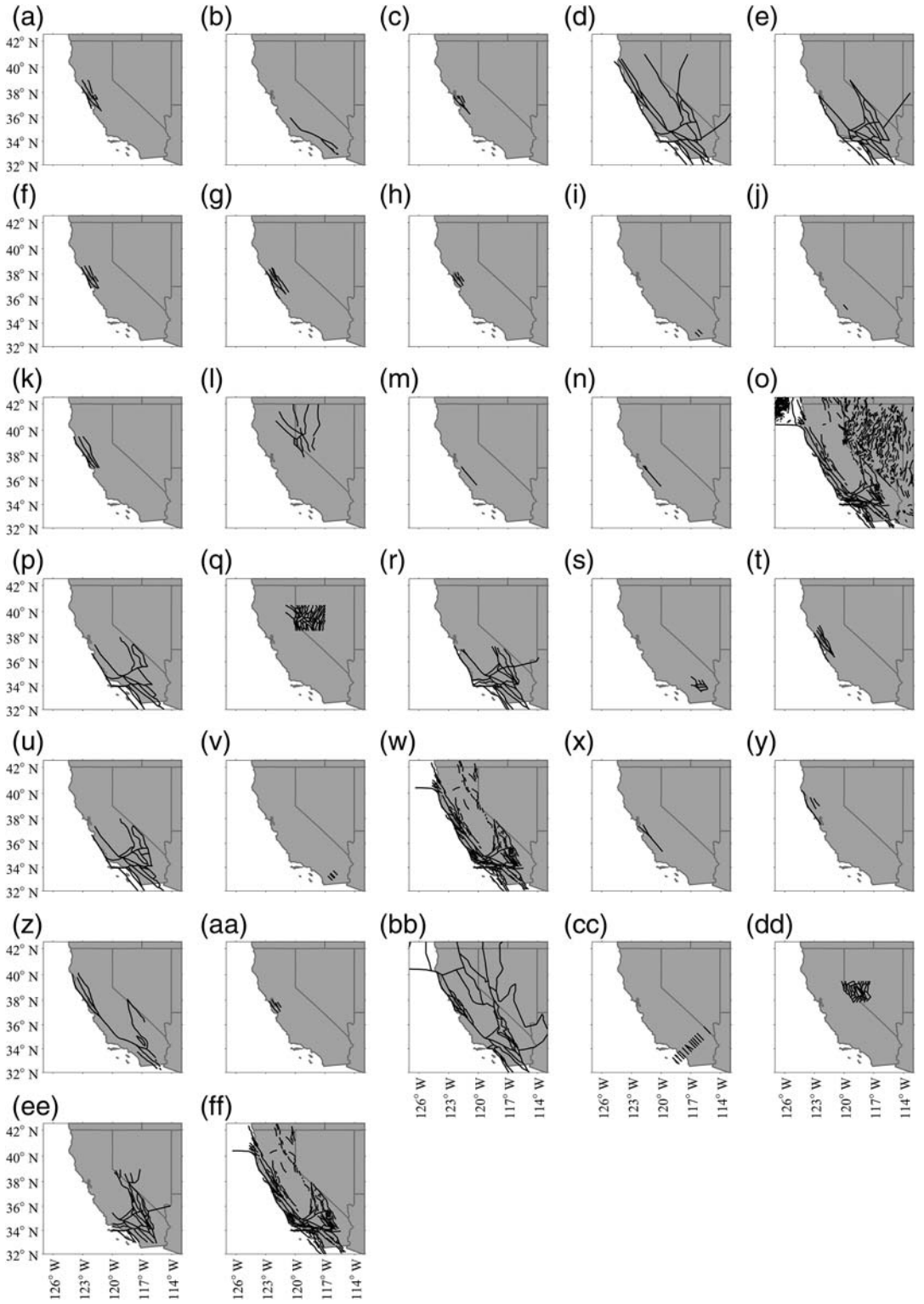

Figure 1. Fault geometries for the 33 geodetic slip-rate models considered (geometry of Johnson, 2013, is used twice, as an elastic model and a viscoelastic model). The spatial extent of a given geometry is limited to the focus area of its respective study. Publications are in chronological order of publication date: (a) Manaker *et al.* (2003), (b) Argus *et al.* (2005), (c) Johanson and Bürgmann (2005), (d) McCaffrey (2005), (e) Meade and Hager (2005), (f) Schmidt *et al.* (2005), (g) d'Alessio *et al.* (2005), (h) Bürgmann *et al.* (2006), (i) Fialko (2006), (j) Schmalzle *et al.* (2006), (k) Funning *et al.* (2007), (l) Hammond and Thatcher (2007), (m) Rolandone *et al.* (2008), (n) Ryder and Bürgmann (2008), (o) Bird (2009), (p) Chuang and Johnson (2011), (q) Hammond *et al.* (2011), (r) Loveless and Meade (2011), (s) Spinler *et al.* (2010), (t) Evans *et al.* (2012), (u) Johnson (2013, elastic), (v) Lindsey and Fialko (2013), (w) Unified California Earthquake Rupture Forecast, version 3.1 (UCERF3.1) (Field *et al.*, 2013), (x) Jolivet *et al.* (2015), (y) Murray *et al.* (2014), (z) Tong *et al.* (2014), (aa) Chaussard *et al.* (2015), (bb) Evans *et al.* (2015), (cc) McGill *et al.* (2015), (dd) Bormann *et al.* (2016), (ee) Evans *et al.* (2016), and (ff) Zeng and Shen (2016).

Table 1
Summary of Models Included in This Compilation

References	Model Style				Rheology		Data (All Use GNSS)		Uncertainty		
	2D Dislocation	3D Dislocation	Block Model	Finite Element	Elastic	Viscoelastic	Geology	InSAR	Formal	Bayesian	Not Included
Manaker *et al.* (2003)		•			•		•		•		
Argus *et al.* (2005)		•			•						•
d'Alessio *et al.* (2005)			•		•				•		
Johanson and Bürgmann (2005)		•			•			•	•		
McCaffrey (2005)			•		•				•		
Meade and Hager (2005)			•		•				•		
Schmidt *et al.* (2005)		•			•			•	•		
Bürgmann *et al.* (2006)		•			•			•	•		
Fialko (2006)	•				• *			•	•		
Schmalzle *et al.* (2006)				•		• *				•	
Funning *et al.* (2007)		•			•			•	•		
Hammond and Thatcher (2007)			•		•				•		
Rolandone *et al.* (2008)		•			•				•		•
Ryder and Bürgmann (2008)		•			•			•	•		
Bird (2009)				•	•						•
Chuang and Johnson (2011)			•			•				•	
Hammond *et al.* (2011)			•		•				•		
Loveless and Meade (2011)			•		•		•		•		
Spinler *et al.* (2010)			•		•				•		
Evans *et al.* (2012)			•		•			•	•		
Johnson (2013)			•		•					•	
			•			•				•	
Lindsey and Fialko (2013)	•				• *			•	•		
Field *et al.* (2013)		•	•		•		•		•		
Jolivet *et al.* (2015)		•			•					•	
Murray *et al.* (2014)		•			•					•	
Tong *et al.* (2014)			•			•		•			•
Chaussard *et al.* (2015)		•			•			•	•		
Evans *et al.* (2015)			•		•		•		•		
McGill *et al.* (2015)	• †				•				•		
Bormann *et al.* (2016)			•		•				•		
Evans *et al.* (2016)			•		•				•		
Zeng and Shen (2016)		•	•		•		•		•		

GNSS, Global Navigation Satellite Systems; InSAR, Interferometric Synthetic Aperture Radar; UCERF, Unified California Earthquake Rupture Forecast.
*These models also consider lateral variations in elastic properties.
†This model includes one fault with a strike that is not perpendicular to the profile.

(Fialko, 2006; Schmalzle *et al.*, 2006) were digitized using GraphClick software. The spatial extent of fault geometry considered for each model is limited to the focus area of the study. For example, the block model of d'Alessio *et al.* (2005) contains a North America block as shown in figures 1 and 3 of that paper, but the study focus is the San Francisco Bay area, so I retain only the bay area faults, as determined by the mapped region (their figs. 2, 4, 5, and 9).

All studies estimate long-term slip rates from GNSS observations (Table 1), nine include GNSS and InSAR observations (Schmidt *et al.*, 2005; Bürgmann *et al.*, 2006; Fialko, 2006; Funning *et al.*, 2007; Ryder and Bürgmann, 2008; Evans *et al.*, 2012; Lindsey and Fialko, 2013; Chaussard *et al.*, 2015; Jolivet *et al.*, 2015), and five studies include geologic slip rates in a joint inversion (e.g., Manaker *et al.*, 2003; Loveless and Meade, 2011; Parsons *et al.*, 2013; Evans *et al.*, 2015; Zeng and Shen, 2016).

Geodetically observed deformation may be attributed partially to sources other than the faults included in a given model. For clarity, I refer to this as OMF deformation, because sources may include postseismic deformation due to viscoelastic relaxation of the mantle and lower crust, permanent crustal deformation, as well as seismogenic faults that are not modeled. I assume that authors dealt with OMF deformation by means they deem most appropriate. These choices reflect variation in model choices that may be reflected in the slip-rate estimates themselves, therefore I do not explicitly distinguish between slip rates estimated within a rigid block model (e.g., Meade and Hager, 2005; Spinler *et al.*, 2010), an earthquake cycle block model (e.g., Chuang and Johnson, 2011; Johnson 2013), a finite-element model (e.g., Bird, 2009), or any other model formulation. Similarly, because fault creep is typically either imposed within a model by decreasing locking depth (e.g., d'Alessio *et al.*,

2005), or estimated as a fraction of the long-term slip rate (e.g., McCaffrey, 2005; Zeng and Shen, 2016), this too represents a modeling choice, and so I do not differentiate between creeping and noncreeping faults within the aggregation. Eventually, translating aggregated slip rates to seismic hazard will require a distinction between faults that release all their accumulated strain in earthquakes and faults that creep fully or partially.

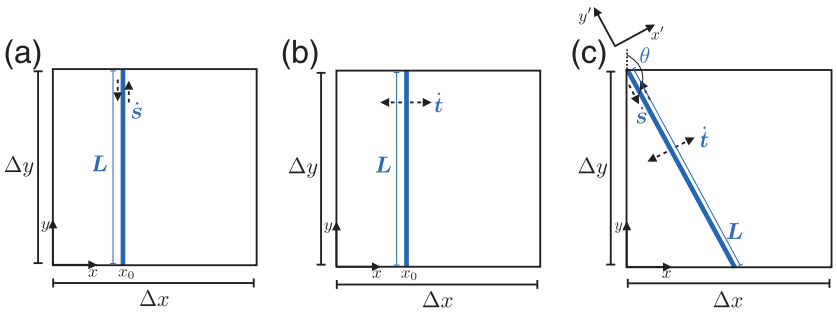

Figure 2. Diagrams describing example breakdowns of model slip rates into spatially averaged velocity gradient tensor (SAVGT): (a) example grid cell with dimensions Δx and Δy, containing a single north–south-striking fault, with strike-slip rate $\dot{s}$ and length L; (b) example grid cell with dimensions Δx and Δy, containing a single east–west-striking fault, with tensile-slip rate $\dot{t}$ and length L; and (c) example grid cell with dimensions Δx and Δy, containing a single fault with strike θ, strike-slip rate $\dot{s}$, tensile-slip rate $\dot{t}$, and length L.

Slip Rates on a Georeferenced Grid

Because fault system geometries differ between models, I combine published geodetic slip-rate estimates on a georeferenced grid. Estimated fault-slip rates are considered on a cell-by-cell basis by comparing the long-term deformation rate predicted by modeled faults. I define the spatially averaged velocity gradient tensor (SAVGT), which is simply the displacement gradient tensor (e.g., Segall, 2010) over time (units of yr^{-1}), containing a component of rigid body rotation that is retained in the analysis. Final calculations are done on a spherical shell to avoid potential bias due to geographic projection; however, I derive the SAVGT here first in the Cartesian coordinate system.

In a Cartesian coordinate system, all faults may be reduced to a 2D representation such that the horizontal component of dip slip is specified as tensile opening or closing; these faults and rates will be referred to as tensile throughout the article but may refer to structures that are physically dipping, and may consequently also produce a vertical component of slip. The gridded representation allows us to assess whether or not different studies result in the same deformation across a given grid cell to compare models spatially, rather than fault by fault. Consideration of the full 3D geometry of faults, including vertical deformation, is necessary for fully assessing the earthquake hazard.

In Cartesian coordinates, the SAVGT is

$$\bar{\mathbf{v}} = \begin{bmatrix} \bar{v}_{xx} & \bar{v}_{xy} \\ \bar{v}_{yx} & \bar{v}_{yy} \end{bmatrix}, \tag{1}$$

in which

$$\bar{v}_{xx} = \frac{1}{A}\iint \frac{\partial \dot{u}}{\partial x} dxdy \tag{2a}$$

$$\bar{v}_{xy} = \frac{1}{A}\iint \frac{\partial \dot{u}}{\partial y} dxdy \tag{2b}$$

$$\bar{v}_{yx} = \frac{1}{A}\iint \frac{\partial \dot{v}}{\partial x} dxdy \tag{2c}$$

$$\bar{v}_{yy} = \frac{1}{A}\iint \frac{\partial \dot{v}}{\partial y} dxdy, \tag{2d}$$

in which $\dot{u}$ is velocity in the x direction, $\dot{v}$ is velocity in the y direction, and A is the area of the grid cell. In this definition, $\bar{v}_{yy}$ and $\bar{v}_{xx}$ represent the two components of extension and $\bar{v}_{xy}$ and $\bar{v}_{yx}$ represent the two components of shear, oriented in the x- and y-parallel orientations, respectively.

All velocities described in this section are long-term tectonic velocities predicted by GSRMs, not observed or predicted geodetic velocities. Similarly, spatially averaged tensors represent long-term tectonic deformation, smoothed at the length scale of the grid spacing.

As a simple example, for a grid cell containing one study with a single strike-slip fault, striking in the y direction, with slip rate $\dot{s}$ (Fig. 2a), there are no velocities in the x direction

$$\dot{u}(x, y) = 0, \tag{3}$$

and velocities in the y direction can be represented by the Heaviside function with amplitude of the slip rate:

$$\dot{v}(x, y) = \dot{s}H(x - x_0). \tag{4}$$

So $\bar{v}_{xx} = \bar{v}_{yy} = \bar{v}_{xy} = 0$, and

$$\bar{v}_{xy} = \frac{\dot{s}}{A}\int_0^{\Delta x}\int_0^{\Delta y} \delta(x - x_0)dxdy = \frac{\dot{s}\Delta y}{A} = \frac{\dot{s}L}{A}, \tag{5}$$

in which $\delta(x)$ is the Dirac delta function, Δx is the width of the grid cell, Δy is the length of the grid cell, and L is the length of the fault.

Similarly, in the case of a grid cell with one study containing a single fault in the same orientation with opening rate $\dot{t}$ (Fig. 2b), $\bar{v}_{xy} = \bar{v}_{yx} = \bar{v}_{yy} = 0$ and

$$\bar{v}_{xx} = \frac{\dot{t}}{A}\int_0^{\Delta x}\int_0^{\Delta y} \delta(x - x_0)dxdy = \frac{\dot{t}\Delta y}{A} = \frac{\dot{t}L}{A}. \tag{6}$$

Because this is a 2D grid, dip-slip rates ($\dot{d}$) are simply converted to horizontal opening rates based on dip φ: $\dot{t} = \dot{d}\cos\varphi$.

Combining these two examples, the SAVGT for a grid cell containing a single north–south-striking fault with both a strike-slip rate $\dot{s}$ and opening rate $\dot{t}$ would have two nonzero components: $\bar{v}_{xx} = \frac{\dot{t}L}{A}$ and $\bar{v}_{yx} = \frac{\dot{s}L}{A}$.

It follows that one may define the average velocity gradient tensor $\bar{\mathbf{v}}'$ in a fault-parallel coordinate system: x' and y', for any arbitrarily oriented fault, deforming by strike-slip and tensile opening (Fig. 2c):

$$\bar{\mathbf{v}}' = \begin{bmatrix} \bar{v}_{x'x'} & \bar{v}_{x'y'} \\ \bar{v}_{y'x'} & \bar{v}_{y'y'} \end{bmatrix} = \begin{bmatrix} \frac{\dot{t}L}{A} & 0 \\ \frac{\dot{s}L}{A} & 0 \end{bmatrix}. \tag{7}$$

The tensor may then be rotated back to the original orientation (or any other orientation of interest). Each component of $\bar{\mathbf{d}}$ may be written out explicitly in a single grid cell due to slip on faults included in a single study, f:

$$\bar{v}^f_{xx} = L_f(\dot{t}_f \cos^2\theta_f + \dot{s}_f \sin\theta_f \cos\theta_f) \tag{8a}$$

$$\bar{v}^f_{xy} = L_f(\dot{t}_f \sin\theta_f \cos\theta_f - \dot{s}_f \sin^2\theta_f) \tag{8b}$$

$$\bar{v}^f_{yx} = L_f(\dot{t}_f \sin\theta_f \cos\theta_f + \dot{s}_f \cos^2\theta_f) \tag{8c}$$

$$\bar{v}^f_{yy} = L_f(\dot{t}_f \sin^2\theta_f + \dot{s}_f \sin\theta_f \cos\theta_f), \tag{8d}$$

in which θ_f is the strike of the fault clockwise from the y axis. For grid cells in which study f includes multiple fault segments, the average displacement rate gradient tensor is simply a sum of the displacement rate gradient tensor over all (N) smaller fault segments:

$$\bar{v}^f_{xy} = \sum_{k=1}^{N} (\bar{v}^f_{xy})_k. \tag{9}$$

As mentioned above, the above equations may be translated onto a spherical shell, removing the need for geographic projection, by replacing L_f with arc length $\tilde{L}_f$, A with quadrangle area $\tilde{A}$, the x and y directions now represent east and north ($\tilde{x}$ and $\tilde{y}$), and θ is the strike of the fault clockwise from north. Equations (2a–d) become

$$\bar{v}^f_{\tilde{x}\tilde{x}} = \frac{1}{\tilde{A}} \sum_{k=1}^{N} \tilde{L}_{f_k}(\dot{t}_{f_k} \cos^2\theta_{f_k} + \dot{s}_{f_k} \sin\theta_{f_k} \cos\theta_{f_k}) \tag{10a}$$

$$\bar{v}^f_{\tilde{x}\tilde{y}} = \frac{-1}{\tilde{A}} \sum_{k=1}^{N} \tilde{L}_{f_k}(\dot{t}_{f_k} \sin\theta_{f_k} \cos\theta_{f_k} - \dot{s}_{f_k} \sin^2\theta_{f_k}) \tag{10b}$$

$$\bar{v}^f_{\tilde{y}\tilde{x}} = \frac{1}{\tilde{A}} \sum_{k=1}^{N} \tilde{L}_{f_k}(\dot{t}_{f_k} \sin\theta_{f_k} \cos\theta_{f_k} + \dot{s}_{f_k} \cos^2\theta_{f_k}) \tag{10c}$$

$$\bar{v}^f_{\tilde{y}\tilde{y}} = \frac{1}{\tilde{A}} \sum_{k=1}^{N} \tilde{L}_{f_k}(\dot{t}_{f_k} \sin^2\theta_{f_k} + \dot{s}_{f_k} \sin\theta_{f_k} \cos\theta_{f_k}). \tag{10d}$$

The average displacement rate gradient tensor in equations (10a–d) is therefore defined by two components of shear deformation (including rotation) and two components of tensile deformation. Left-lateral deformation is defined here as positive; right lateral is defined as negative. Similarly, tensile deformation is defined as positive and convergence is negative. Furthermore, with the average displacement rate gradient tensor defined in a north–south coordinate system, it is trivial to define an average strain-rate tensor and average rotation-rate tensor. Because California is characterized by a large-scale strike-slip system and is therefore dominated by simple shear, in which strain and rotation both contribute to observed deformation, I prefer not to separate the strain and rotation tensors in favor of the more general velocity gradient tensor.

One may consider deformation in terms of slip rates (mm/yr), for comparison with geologic slip rates, by multiplying the displacement rate gradient by grid cell area $\tilde{A}$, and dividing by the corresponding grid cell arc length in the east ($\Delta\tilde{x}$) or north ($\Delta\tilde{y}$) direction:

$$\dot{\mathbf{s}}^f_{\tilde{\mathbf{x}}} = \frac{-\bar{v}^f_{xy}\tilde{A}}{\Delta\tilde{x}} \tag{11a}$$

$$\dot{\mathbf{s}}^f_{\tilde{\mathbf{y}}} = \frac{\bar{v}^f_{yx}\tilde{A}}{\Delta\tilde{y}} \tag{11b}$$

$$\dot{\mathbf{t}}^f_{\tilde{\mathbf{x}}} = \frac{\bar{v}^f_{xx}\tilde{A}}{\Delta\tilde{x}} \tag{11c}$$

$$\dot{\mathbf{t}}^f_{\tilde{\mathbf{y}}} = \frac{\bar{v}^f_{yy}\tilde{A}}{\Delta\tilde{y}}. \tag{11d}$$

The velocity gradient and slip-rate components may all be subsequently rotated into an orientation of interest, such as, for example, the Pacific–North America (PA–NA) plate direction of 145° (DeMets *et al.*, 2010).

Results

Applying the gridding procedure to all 33 GSRMs produces a suite of SAVGTs within each grid cell, which represents the range of modeled tectonic deformation. The grid is defined in geographic coordinates to align the grid with geographic boundaries and landmarks, although the method may be applied to any grid geometry or geographic projection of interest. The latitude dimension is scaled by 0.8 relative to the longitude dimension so that grid cells are approximately square. A grid of 542 cells with dimensions 0.4° in the

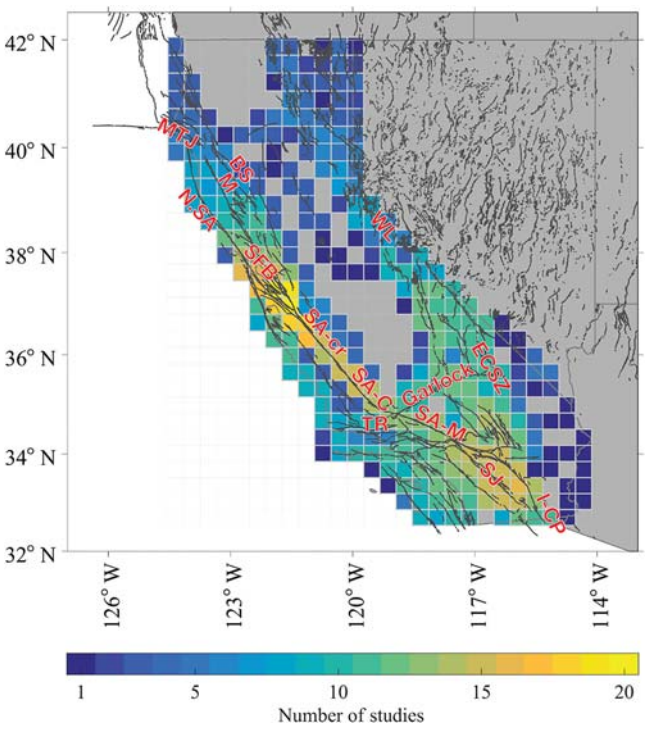

Figure 3. Grid over which slip-rate models are combined and defined in geographic coordinates. Grid cells span 0.40° in the longitude direction, and 0.32° in the latitude direction. Colors represent the number of geodetic studies contained within each cell. Faults (dark gray) are from the U.S. Geological Survey Quaternary fault and fold database. Select faults and regions labeled: BS, Bartlett Springs; ECSZ, eastern California shear zone; I-CP, Imperial/Cerro Prieto faults; M, Maacama fault; MTJ, Mendocino Triple Junction; N.SA, northern San Andreas fault; SA-C, San Andreas fault, Carrizo segment; SA-cr, San Andreas fault, creeping segment; SA-M, San Andreas fault, Mojave segment; SFB, San Francisco Bay area; SJ, San Jacinto fault; TR, Transverse Ranges; WL, Walker Lane.

longitude direction and 0.32° in the latitude direction (Fig. 3) produces the best agreement with geologic slip rates (discussed in detail in the Grid Size Assessment section) and is interpreted to represent the most appropriate length scale for compiling slip-rate estimates. Two alternative grids, a coarse grid of 263 cells with dimensions 0.6° in the longitude direction and 0.48° in the latitude direction and a dense grid of 2121 cells with dimensions 0.2° in the longitude direction and 0.16° in the latitude direction are included in Ⓔ Figure S1 (available in the electronic supplement to this article) for comparison. Because the grid is defined in geographic coordinates, grid cells in the southernmost row cover 13% more surface area than grid cells in the northernmost row. However, this difference is small and the spatial averaging described in the Slip Rates on a Georeferenced Grid section should mitigate any potential distortion due to variable grid sizes.

It is important to note that the 33 models included in this analysis may not be considered independent because some represent subsequent studies from the same research groups (e.g., Meade and Hager, 2005; Loveless and Meade, 2011; Evans *et al.*, 2015) including two models from one publication (Johnson, 2013). Results from Hammond *et al.* (2011) and Lindsey and Fialko (2013) may be considered updates of previous studies: Hammond and Thatcher 2007 and Fialko (2006), respectively. However, because this is the first quantitative compilation of geodetic slip rates in California, I focused on simple and straightforward metrics to summarize slip rate and uncertainty: the mean and standard deviation of estimated slip rates within each grid cell, with each study given equal weight. Standard deviation is only one of many potential metrics for assessing variability in a distribution, and I use it here because it is in the same units as the distribution values and is easily interpretable. The approach may be readily extended to exclude older studies or to include weighting and alternative statistics. Finally, I only consider standard deviations in grid cells containing more than one model, so that all standard deviations are nonzero.

The mean values over all 33 models of each component of the SAVGT from equations (10a–d) represent the community-averaged long-term deformation rate within each grid cell, and standard deviation represents uncertainty on that rate (Fig. 4 and Ⓔ Figs. S2–S3). In all four components of the mean SAVGT ($\bar{v}_{\tilde{x}\tilde{x}}$, $\bar{v}_{\tilde{x}\tilde{y}}$, $\bar{v}_{\tilde{y}\tilde{x}}$, $\bar{v}_{\tilde{y}\tilde{y}}$), the highest deformation rates ($> 1 \times 10^{-6}$ yr^{-1}) occur along the San Andreas fault system. In eastern California, where the eastern California shear zone accommodates ~25% of PA–NA relative motion (e.g., Sauber *et al.*, 1994; Dixon *et al.*, 2003), deformation is more diffuse, with average rates up to 4×10^{-7} yr^{-1}. Standard deviation on the SAVGT correlates roughly with deformation rate, with highest standard deviations of 1.5×10^{-7} to 2.0×10^{-7} yr^{-1} (in the $\bar{v}_{\tilde{x}\tilde{y}}$ component) in northwestern and southeastern most California. The average standard deviation across all components in all grid cells on the SAVGT is 3.51×10^{-8} yr^{-1}.

Geodetic Slip Rates

The SAVGT results are especially informative when scaled by grid cell area to represent spatially averaged slip rates (equations 11a–d), and then rotated from the east–north coordinate system into the PA–NA-parallel plate direction of 145° (DeMets *et al.*, 2010) (Fig. 5 and Ⓔ Figs. S4–S5). I use the same rotation in every grid cell for simplicity, although it would be trivial to apply individual rotations to each cell to reflect the slight variation in PA–NA relative plate direction across California. This orientation highlights plate-boundary-parallel strike-slip motion of up to $\dot{\mathbf{s}} = -35$ mm/yr (right lateral), with standard deviations of 2–5 mm/yr along the central San Andreas fault, and plate-boundary-perpendicular left-lateral strike-slip motion along the Garlock fault of up to $\dot{\mathbf{s}} = 7$ mm/yr, with standard deviations > 4 mm/yr (Fig. 5). Plate-boundary-perpendicular extension in the eastern California shear zone varies across the region with mean rates of $\dot{\mathbf{t}} = -0.5$–0.5 mm/yr, and standard deviations of up to 5 mm/yr. Plate-boundary-parallel convergence rates (negative tensile deformation) of $\dot{\mathbf{t}} = -12$ mm/yr, with standard deviations of 5 mm/yr,

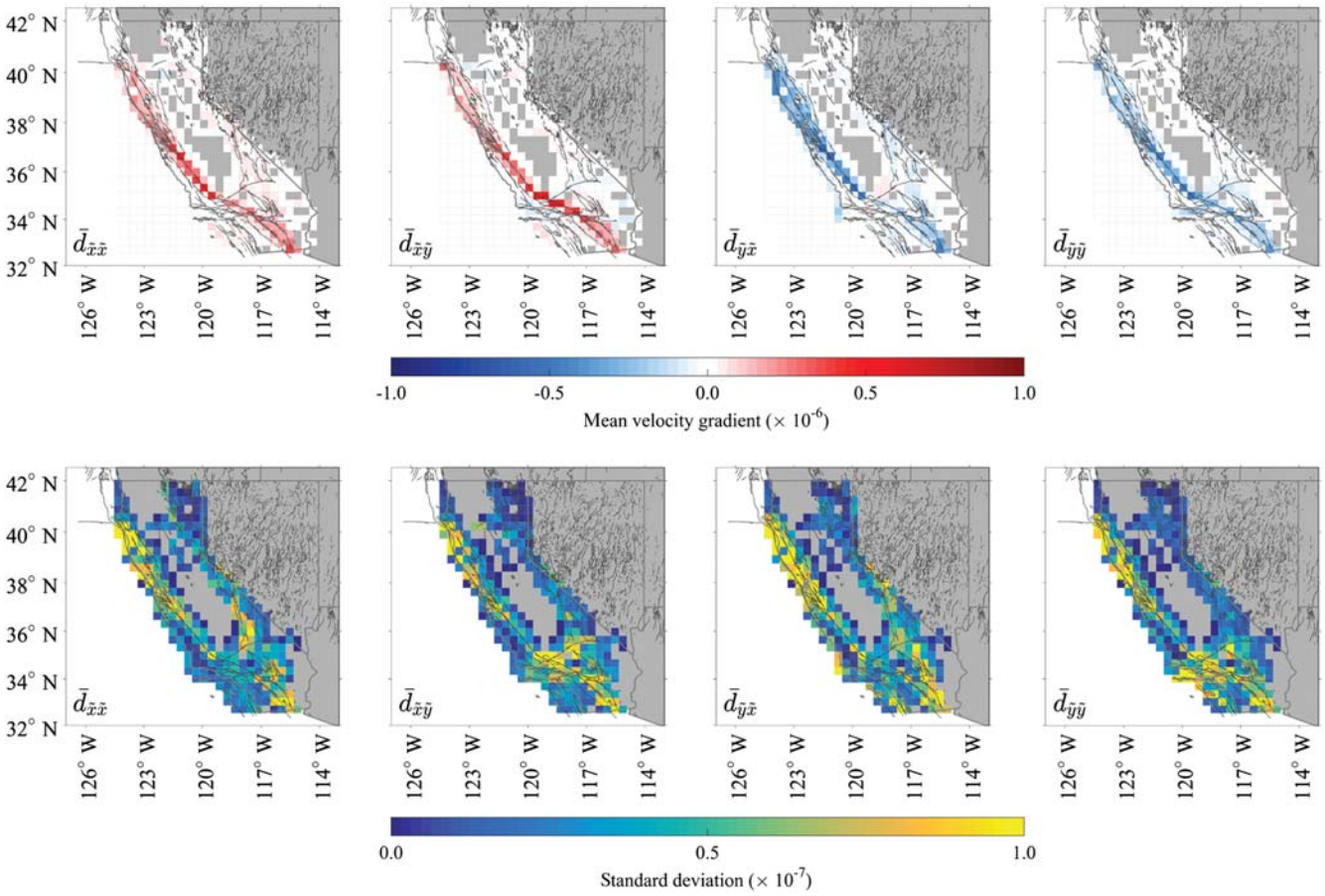

Figure 4. (Top row) Mean values over all studies of each of the four components of the SAVGT; (bottom row) standard deviation over all studies of each of the four components of the SAVGT.

are apparent through Big Bend in California. The distribution of standard deviations follows that of the SAVGT, with highest standard deviations in northern California and in the southeastern most corner of the state (5–7 and 4–9 mm/yr, respectively). The average standard deviation across all components of slip rate is 1.3 mm/yr.

Comparison with Geologic Slip Rates

A common goal of geodetic slip-rate estimation is to compare slip rates derived from geodetic methods with slip rates estimated from geology. I use the statistics of deformation described above to compare geologic and geodetic slip rates. I consider 101 strike-slip geologic slip rates from the UCERF3 (Field *et al.*, 2013) geologic slip-rate catalog in Appendix B of Dawson and Weldon (2013) for which site location and strike are reported. For each geologic slip rate, the geodetic slip-rate estimates in the corresponding grid cell are rotated to the strike of the geologic slip rate, to directly compare the geologic rate with the mean rotated geodetic rate (Fig. 6). Geologic uncertainties (horizontal error bars in Fig. 6) are from UCERF3 Appendix B (Dawson and Weldon, 2013). Geodetic uncertainties (vertical error bars in Fig. 6) represent the standard deviation of the population of the geodetic studies in that grid cell. If geologic and geodetic slip rates agree, a line fit to this comparison should fall on the 1:1 line. A weighted linear fit (York *et al.*, 2004) (assuming geologic uncertainties represent one standard deviation), with intercept fixed at zero, produces a slope of 1.02. Geologic slip rates from UCERF3 and their corresponding geodetic slip rates from this study are reported in Table 2.

Compared at this grid spacing, 73 geologic and geodetic slip rates agree within uncertainty, 23 geodetic slip rates are higher than geologic rates, and 5 geodetic slip rates are lower than geologic rates. Although more geodetic slip rates exceed geologic rates, four geologic slip rates (on the Mojave segment of the San Andreas fault) are much higher (180%–250%) in magnitude than the corresponding geodetic rates.

Grid Size Assessment

The results of this analysis depend on the dimensions and location of the geographic grid: on a grid that is too coarse, a single grid cell may average over multiple faults with different behaviors, in which case a geologic rate on any faults within the cell would disagree with the compiled geodetic rates. A grid that is too small may not capture all possible model representations of a single fault, and therefore

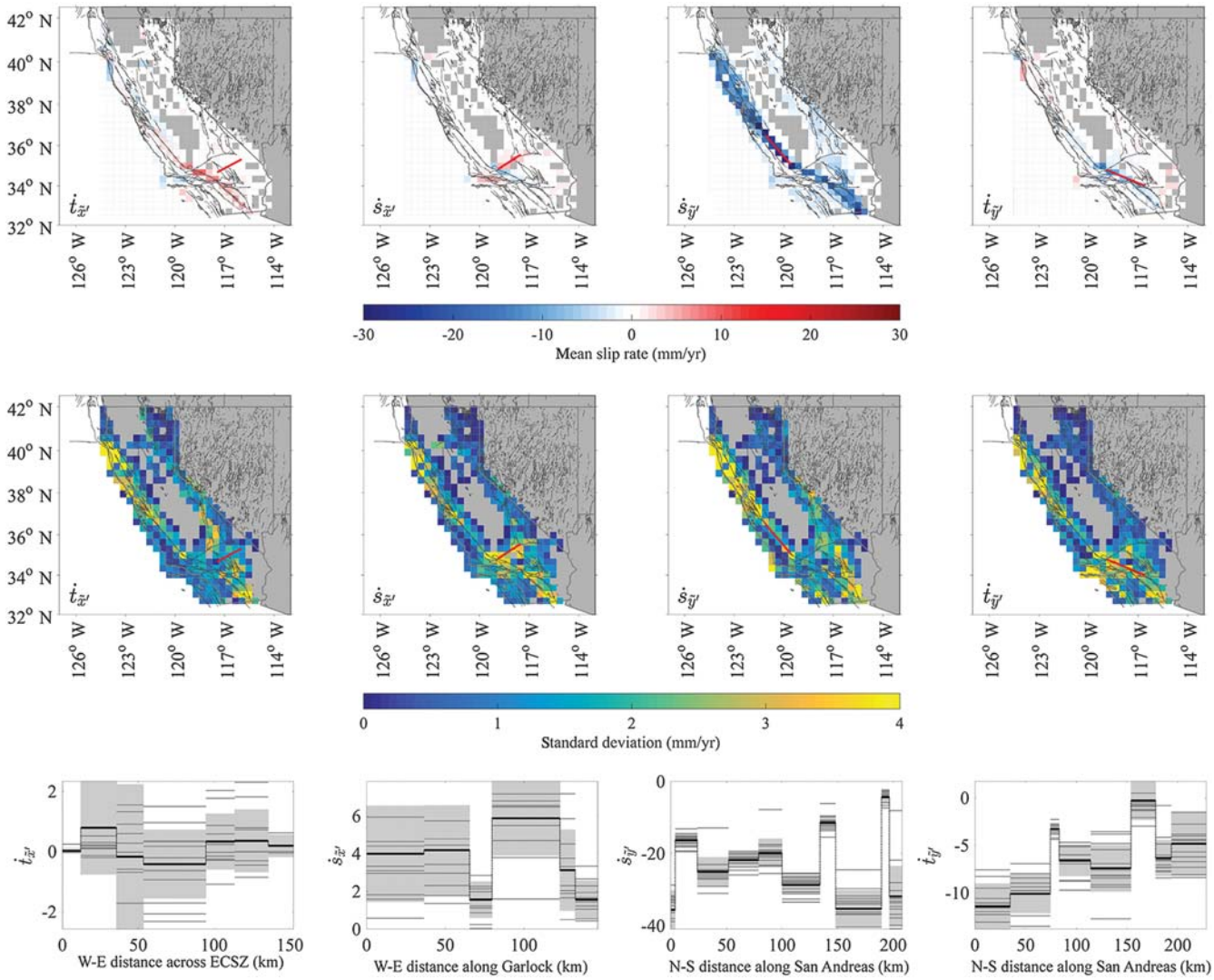

Figure 5. (Top row) Mean values over all studies of each of the four slip-rate components, calculated from the SAVGT (Fig. 4) and rotated parallel to the Pacific–North America (PA–NA) plate motion of 145° (DeMets *et al.*, 2010). Positive tensile rates indicate opening; positive strike-slip rates are left lateral. Red lines identify locations of slip profiles in bottom row. (Middle row) Standard deviation over all studies of each of the four slip-rate components, calculated from the deformation gradient tensor (Fig. 4) and rotated parallel to the PA–NA plate motion of 145°; (bottom row) selected slip profiles through each slip component. The black line is the mean value in each grid cell along the profile, the gray area represents the standard deviation, and thin gray lines represent each study's slip estimate in each grid cell, also rotated parallel to the PA–NA plate motion of 145°. Note different scaling in x and y axes.

would not capture the suite of relevant geodetic slip rates. In other words, an optimized spacing may represent the length scale of epistemic uncertainty in fault system geometry from geodetic observations. To determine the most appropriate grid spacing, I benchmark against geologic slip rates. To do this, I test nine successively coarser grids between 0.1° and 0.5° longitude spacing to find the grid dimensions for which the integrated geodetic rates are most consistent with geologic rates. For each grid, I assess the geologic–geodetic comparison described in the Comparison with Geologic Slip Rates section. Because geodetically estimated long-term slip rates are expected to be compatible with geologic slip rates, I select the grid spacing in which the weighted linear fit produces a line with slope closest to 1. This occurs at a longitude dimension of 0.4° (Ⓔ Fig. S6). For comparison, grid dimensions of 0.2° (best-fitting slope 0.93) and 0.6° (best-fitting slope 1.08) are included in Ⓔ Figures S7–S8.

Potency

This analysis of previous geodetic deformation rates focuses on slip rate for direct comparison with geologic observations because most studies of geodetic deformation primarily report and discuss geodetic estimates of slip rate. Geodetic methods may be more sensitive to fault potency (geometric moment), which is fault-slip rate multiplied by effective locking depth, than to slip rate alone (Johnson *et al.*, 1994; Maurer and Johnson, 2014; Tong *et al.*, 2014; Maurer

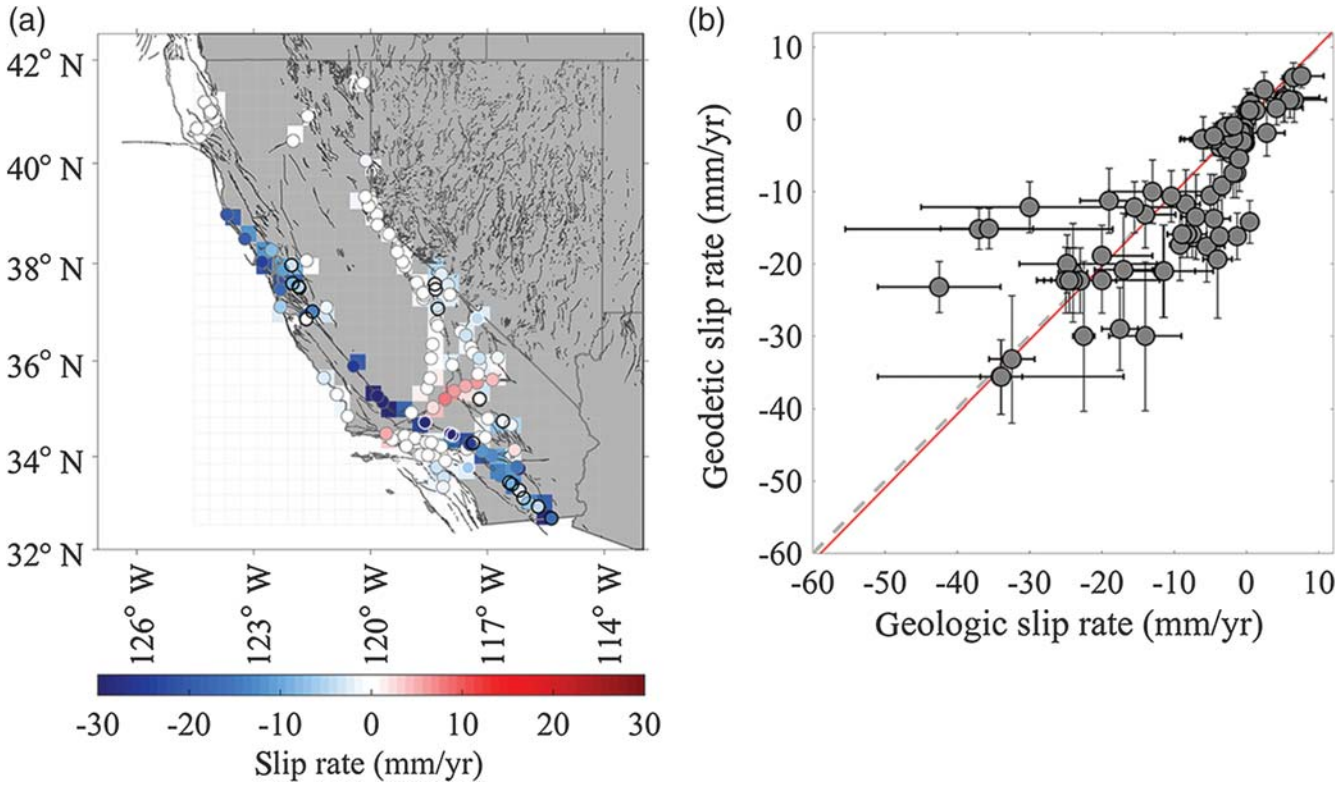

Figure 6. Direct comparison of geodetic and geologic strike-slip rates: (a) locations of geologic slip rates (circles), superimposed on corresponding grid cells and mean geodetic slip rate in that grid cell, in the same orientation as the geologic slip rate. Circle fill colors correspond to estimated strike-slip rate; black outline indicates an estimated geodetic rate higher than geologic rate; white outline indicates estimated geodetic rate lower than geologic rate. (b) Graphical comparison of rates. Geologic slip rates and horizontal error bars are the estimated rate and reported geologic uncertainty. Geodetic slip rates and vertical error bars are the mean rate in the corresponding grid cell in the orientation of the geologically estimated rate and the standard deviation over geodetic slip rates, respectively. The dashed gray line is 1:1; the solid red line is a weighted linear fit to the geologic and geodetic rates, with slope 1.02.

et al., 2017). However, estimates of geodetic slip rate typically require an assumed locking depth, which is often poorly resolved and may vary considerably along strike (e.g., Smith-Konter *et al.*, 2011). Given an estimated locking depth in addition to slip rate for each of the 33 GSRMs, it would be possible to determine a total potency rate predicted by each study in each cell. This value would represent the potency accumulation rate if all faults in the cell were fully locked between the locking depth and the surface. Authors may differ in their approach to partial creep, representing model creep with changes in locking depth, burial depth, and/or coupling fraction, so to maintain a general representation of deformation that is consistent with the SAVGT, I refer to the average potency rate per unit depth ($\overline{\dot{\mathbf{P}}_0}$) which may be multiplied by a coupling fraction (e.g., Zeng and Shen, 2014) along with locking depth to calculate a potency accumulation rate. Both the locking depth and the coupling fraction have additional uncertainties associated with them that would need to be accounted for in such an analysis.

The magnitude of the SAVGT in each grid cell is equivalent to the average potency rate per unit depth due to study f (Fig. 7 and Ⓔ Figs. S9–S10), which is independent of fault orientation and provides a single, physically intuitive measure of the amount of deformation in each grid cell:

$$\overline{\dot{\mathbf{P}}_0^f} = \frac{1}{\tilde{A}_c}\sum_{k=1}^{N} s_{f_k}\tilde{L}_{f_k}. \tag{12}$$

The horizontal potency rate of dipping faults is scaled by $\cos\varphi$ to account for greater fault width per unit depth. As a simple example, assuming total locking between the surface and 10 km on grid cells that do not contain the creeping segment of the San Andreas fault (Fig. 3), the total potency accumulation rate in California would be 1.91×10^{19} m^3/yr, equivalent to an $\mathbf{M} \approx 8.1$ (assuming a shear modulus of 30 GPa to convert potency to magnitude) earthquake every 100 yrs. For comparison, the moment release rate over the last 100 yrs is equivalent to $\mathbf{M} \approx 8.0$ (considering earthquakes of $\mathbf{M} \geq 4.0$; Advanced National Seismic System catalog data accessed through the Northern California Earthquake Data Center; see Data and Resources).

As with slip rate, the highest potency rates per unit depth occur along the San Andreas fault, with a maximum mean $\overline{\dot{\mathbf{P}}_0}$ of 1357 m^3/yr/m on the Carrizo segment (Fig. 7). The distribution of mean potency is approximately lognormal

Table 2
Geologic–Geodetic Slip-Rate Comparison (Right-Lateral Positive)

Fault Name	UCERF3 Geologic Rate ± Uncertainty (mm/yr)	Mean Geodetic Rate ± St. Dev. (mm/yr)
Ash Hill	0.30 ± 0.10	1.20 ± 1.25
Ash Hill	0.45 ± 0.05	1.77 ± 1.58
Blackwater fault	0.49 ± 0.04	3.08 ± 2.22
Calaveras (central) 2011 CFM	14.00 ± 5.00	29.99 ± 10.26
Calaveras (north) 2011 CFM	5.50 ± 2.50	17.58 ± 4.94
Calaveras (north) 2011 CFM	5.50 ± 0.50	17.58 ± 4.94
Calaveras (north) 2011 CFM	5.00 ± 2.00	10.54 ± 2.93
Calico-Hidalgo	1.40 ± 0.40	7.42 ± 3.44
Calico-Hidalgo	1.80 +0.80,−0.30	7.42 ± 3.44
Cleghorn	−0.45 ± 0.15	14.19 ± 2.95
Concord 2011 CFM	3.40 ± 0.30	9.19 ± 4.63
Death Valley (Black Mountains frontal)	1.73 ± 1.00	0.91 ± 0.62
Death Valley (Fish Lake Valley)	2.17 ± 0.40	4.76 ± 4.22
Death Valley (Fish Lake Valley)	2.69 ± 0.40	4.08 ± 1.40
Death Valley (north)	4.50 + 1.60,−1.40	2.35 ± 0.71
Elsinore (Glen Ivy) rev	4.45 + 4.85,−3.15	2.78 ± 1.06
Elsinore (Glen Ivy) rev	6.00 + 6.20,−3.20	2.78 ± 1.06
Elsinore (Glen Ivy) rev	5.60 ± 0.30	2.78 ± 1.06
Elsinore (Glen Ivy) rev	6.20 + 5.00,−2.40	2.78 ± 1.06
Garlock (central)	−6.50 ± 1.50	−5.78 ± 2.06
Garlock (central)	−5.10 ± 0.30	−2.61 ± 3.00
Garlock (central)	−6.60 ± 1.20	−2.61 ± 3.00
Garlock (central)	−5.30 + 1.00,−2.50	−2.61 ± 3.00
Garlock (central)	−6.00 + 5.00,−1.00	−2.70 ± 2.49
Garlock (central)	−6.00 + 5.00,−1.00	−2.70 ± 2.49
Garlock (west)	−2.45 ± 0.85	−4.11 ± 2.43
Garlock (west)	−7.60 + 3.10,−2.30	−5.98 ± 1.61
Hayward (north) 2011 CFM	10.40 ± 2.00	10.66 ± 3.56
Hayward (south) 2011 CFM	9.20 ± 1.40	17.37 ± 4.93
Hollywood	−0.30 ± 0.20	−1.05 ± 2.60
Honey Lake 2011 CFM	1.70 ± 0.60	1.75 ± 0.82
Hosgri	1.65 ± 0.95	2.79 ± 2.26
Hosgri	4.30 ± 3.50	2.79 ± 2.26
Hosgri	2.15 ± 1.25	2.79 ± 2.26
Hunter Mountain–Saline Valley	0.92 ± 0.94	2.19 ± 0.94
Hunter Mountain–Saline Valley	3.16 ± 0.35	2.12 ± 0.93
Imperial	17.50 ± 2.50	29.01 ± 5.74
Lenwood–Lockhart–Old Woman Springs	0.80 ± 0.20	1.78 ± 1.04
Little Lake	0.60 ± 0.10	2.43 ± 2.12
Malibu Coast alt 1	−0.03 ± 0.02	−1.13 ± 3.10
Malibu Coast alt 1	−1.30 ± 0.50	−1.23 ± 3.03
Malibu Coast alt 1	−0.02 + 0.01,−0.00	0.03 ± 2.24
Newport-Inglewood alt 1	0.48 ± 0.24	1.03 ± 2.93
Ortigilita (north)	1.50 ± 1.00	2.82 ± 1.92
Owens Valley	0.24 ± 0.04	2.61 ± 1.97
Owens Valley	3.65 ± 0.85	2.71 ± 1.38
Owl Lake	−4.15 ± 3.65	−1.54 ± 2.29
Palos Verdes	3.65 + 0.65,−0.95	3.89 ± 1.74
Palos Verdes	3.00 + 0.80,−0.50	3.55 ± 1.52
Palos Verdes	3.30 ± 0.30	1.35 ± 2.19
Panamint Valley	1.82 ± 0.50	2.62 ± 1.11
Panamint Valley	2.34 ± 1.50	1.08 ± 1.43
Panamint Valley	2.86 ± 0.70	1.08 ± 1.43
Pinto Mountain	−2.80 ± 2.50	1.89 ± 3.16
Pisgah-Bullion–Mesquite Lake	1.00 ± 0.20	5.46 ± 4.49
Polaris 2011 CFM	0.40 + 0.50,−0.40	1.43 ± 1.56
Rodgers Creek–Healdsburg 2011 CFM	8.40 ± 2.00	11.74 ± 4.75
Russ 2011 CFM	0.14 ± 0.10	0.17 ± 1.51
Russ 2011 CFM	0.14 ± 0.10	0.17 ± 1.51

(*continued*)

(Fig. 8), although it is unlikely that any large potency faults have been overlooked (e.g., Meade, 2007). The potency distribution is such that 95% of California potency (slip rates $>\sim$0.5 mm/yr) occurs within 31% of the area covered by the grid, and within 52% of the active area in which mean potency rates are nonzero (Fig. 8). These results suggest slightly more distributed deformation than a previous assessment of the on-fault potency distribution in southern California (Meade, 2007), in which 97% of slip in southern California was estimated to occur on structures slipping >1 mm/yr, although any direct comparison of results is difficult given the spatial averaging of the approach used here. The average standard deviation on $\overline{\dot{\mathbf{P}}_0}$ is 122.5 $m^3/yr/m$, and the log mean is 73 $m^3/yr/m$ (Fig. 8). As with standard deviation on slip rate, the standard deviation on $\overline{\dot{\mathbf{P}}_0}$ varies geographically, with the highest values of 500–623 $m^3/yr/m$ near the Mendocino triple junction, the Transverse Ranges, and at the Imperial–Cerro Prieto intersection along the California–Mexico border.

Discussion

The standard deviations of SAVGT, slip rate, and potency as presented in Figures 4, 5, and 7 may be considered proxies for the epistemic uncertainties in geodetically modeled deformation. California is an ideal candidate for this analysis because a large area (285 grid cells, ~372,000 km^2) of California has been modeled in two or more geodetic slip-rate studies. Although the slip rates may not be fully independent, in many locations, it is fair to assume that slip-rate models span the range of valid model choices, and therefore this range may be a reasonable proxy for epistemic uncertainty. It may be appropriate for future geodetic slip-rate estimates to be presented in the context of the range of previously estimated slip rates as a metric of the uncertainty in that geographic area.

Standard Deviation as a Proxy for Uncertainty

Systematically comparing geodetic slip rates enables the assessment of variability between published models. Using

Table 2 (*Continued*)

Fault Name	UCERF3 Geologic Rate ± Uncertainty (mm/yr)	Mean Geodetic Rate ± St. Dev. (mm/yr)
San Andreas (Carrizo) rev	34.00 ± 17.00	35.63 ± 5.11
San Andreas (Carrizo) rev	33.90 ± 2.90	35.65 ± 5.11
San Andreas (Carrizo) rev	32.45 ± 3.15	33.19 ± 8.78
San Andreas (Coachella) rev	30.00 ± 15.00	12.15 ± 3.52
San Andreas (Coachella) rev	15.50 + 6.50,−3.50	12.16 ± 3.54
San Andreas (Mojave north)	42.50 ± 8.50	23.20 ± 3.54
San Andreas (Mojave south)	37.00 ± 18.50	15.19 ± 2.82
San Andreas (Mojave south)	35.60 + 6.10,−6.70	15.12 ± 2.78
San Andreas (North Branch Mill Creek)	2.10 ± 0.50	0.84 ± 1.59
San Andreas (North Coast) 2011 CFM	20.00 + 7.00,−1.00	18.88 ± 4.22
San Andreas (North Coast) 2011 CFM	19.00 ± 4.00	11.26 ± 4.48
San Andreas (North Coast) 2011 CFM	24.00 ± 2.00	21.23 ± 6.82
San Andreas (Parkfield)	24.80 + 12.40,−6.60	20.01 ± 4.03
San Andreas (Peninsula) 2011 CFM	17.00 ± 4.00	20.82 ± 7.82
San Andreas (San Bernardino north)	20.00 + 8.00,−7.00	22.26 ± 4.55
San Andreas (San Bernardino north)	23.00 + 5.00,−2.00	22.31 ± 4.51
San Andreas (San Bernardino north)	24.00 + 6.00,−5.00	22.29 ± 4.53
San Andreas (San Bernardino north)	25.00 + 6.00,−4.00	22.26 ± 4.55
San Andreas (San Bernardino north)	24.00 ± 4.00	22.31 ± 4.49
San Andreas (San Bernardino north)	24.50 ± 3.50	22.30 ± 4.47
San Andreas (San Bernardino south)	11.55 + 6.95,−5.25	21.01 ± 6.40
San Andreas (San Bernardino south)	11.40 + 4.30,−4.40	21.01 ± 6.40
San Andreas (San Bernardino south)	13.00 + 7.00,−6.00	10.01 ± 4.39
San Andreas (Santa Cruz Mountains) 2001 CFM	22.50 ± 1.50	30.00 ± 10.33
San Diego trough north alt 1	1.50 ± 0.30	1.09 ± 2.84
San Gregorio (north) 2011 CFM	6.00 ± 3.00	2.68 ± 3.04
San Jacinto (Anza) rev	14.00 + 4.20,−2.70	13.18 ± 4.61
San Jacinto (Borrego)	4.50 ± 2.25	13.76 ± 6.12
San Jacinto (Clark) rev	1.30 ± 0.40	16.18 ± 3.21
San Jacinto (Clark) rev	3.70 + 1.10,−1.00	16.18 ± 3.21
San Jacinto (Clark) rev	7.50 + 2.00,−1.60	15.92 ± 3.20
San Jacinto (Clark) rev	8.20 + 1.80,−2.80	15.92 ± 3.20
San Jacinto (Clark) rev	8.90 ± 2.00	15.92 ± 3.20
San Jacinto (Superstition Hills)	4.00 ± 2.00	19.36 ± 8.15
San Jacinto (Superstition Mountain)	7.00 ± 2.00	13.50 ± 5.87
Santa Monica alt 1	−0.43 ± 0.25	−1.24 ± 2.56
Santa Ynez (east)	−5.12 ± 4.97	−3.00 ± 1.54
Simi–Santa Rosa	−0.61 ± 0.20	−2.17 ± 1.42
White Mountains	0.18 ± 0.05	3.25 ± 2.37
White Mountains	0.25 ± 0.05	3.30 ± 2.36
White Mountains	0.33 ± 0.10	3.30 ± 2.36
Zayante-Vergeles	0.52 + 0.50,−0.56	3.47 ± 1.94

CFM, Community fault model.

standard deviation as a proxy for model uncertainty, the standard deviations of 1.5–4 mm/yr may suggest that model uncertainties are of similar magnitude. Standard deviations vary geographically, with high values near complex fault intersections and in regions with only a few published studies. For example, models of the geometrically simple central San Andreas fault show relatively little variability (standard deviations of <1 mm/yr, even given the many estimates of slip rate [14–20 studies] in this region; Figs. 3 and 5). Geometrically complex regions tend to have high model uncertainty, with standard deviations of 5–10 mm/yr near the Mendocino triple junction, up to 5–6 mm/yr in the San Francisco Bay area, and 5–8 and 5–9 mm/yr near the San Andreas intersections with the Garlock and San Jacinto faults, respectively (Fig. 5).

Regions in which standard deviations are high, but where the number of available geodetically estimated slip rates is low, may be regions in which further investigation may be particularly beneficial to reducing epistemic uncertainties. For example, relatively high standard deviations of >6 mm/yr on plate-boundary-parallel shear (Fig. 5) in northernmost California near the Maacama fault correspond to eight studies (Fig. 3). Similarly, standard deviations of 4–6 mm/yr on plate-boundary-parallel extension in the Transverse Ranges are based on six studies (Figs. 3 and 5). In comparison, 20 models constrain slip rate on the central San Andreas fault.

Reported uncertainties on estimated slip rates are included in 27 GSRMs. I compare each of these reported uncertainties with the standard deviation among all estimated slip rates in respective grid cells, rotated into the same orientation as the model fault (Fig. 9). Most models calculate uncertainties with propagation of the error covariance matrix, although five of the studies considered estimated geodetic slip rates within a Bayesian framework (their uncertainties are represented by the posterior distribution over many models), and four models do not include their uncertainties (Table 1).

In general, standard deviations on slip rate span a wider range than reported uncertainties, with the latter ranging from 0.1 to 5 mm/yr (with one very large reported uncertainty of 34 mm/yr according to Funning *et al.*, 2007), and the former from 0.1 to 10 mm/yr (Fig. 9). With the exception of the reported uncertainties from Jolivet *et al.* (2015), which estimates slip rates while varying model elastic structure, there is little obvious distinction in the magnitude of reported uncertainty from error propagation and those derived from Bayesian methods. Although Bayesian methods interrogate a large suite of possible model realizations, they do not seem to provide a systematically larger estimate of total uncertainty than error propagation methods when sampling within a single fault geometry and elastic structure.

In addition to fault geometry, another potential source of uncertainty is bias due to incorrectly accounting for time-dependent viscoelastic relaxation (e.g., Hearn *et al.*, 2013). Four studies estimate geodetic slip rates within time-dependent finite-element (Schmalzle *et al.*, 2006) or block

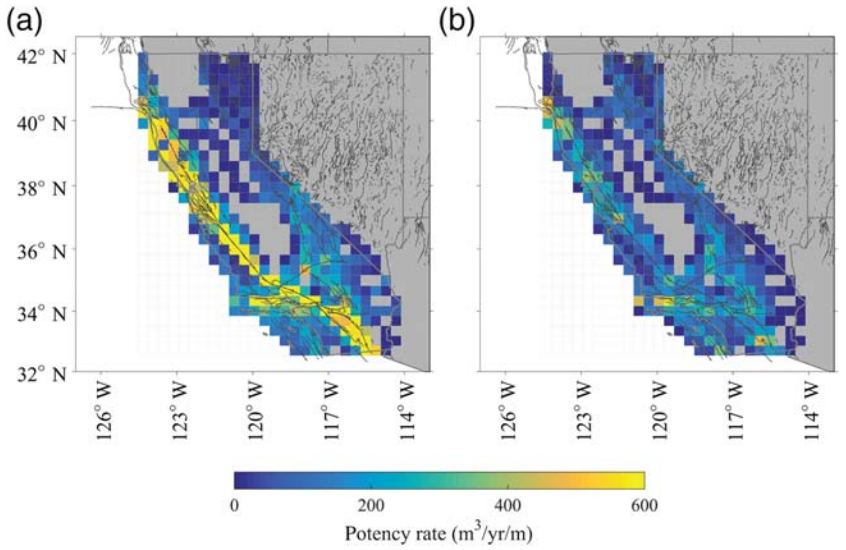

Figure 7. Summary of estimated potency (geometric moment) accumulation rate per unit depth over all studies considered. (a) Mean value and (b) standard deviation of potency accumulation rate.

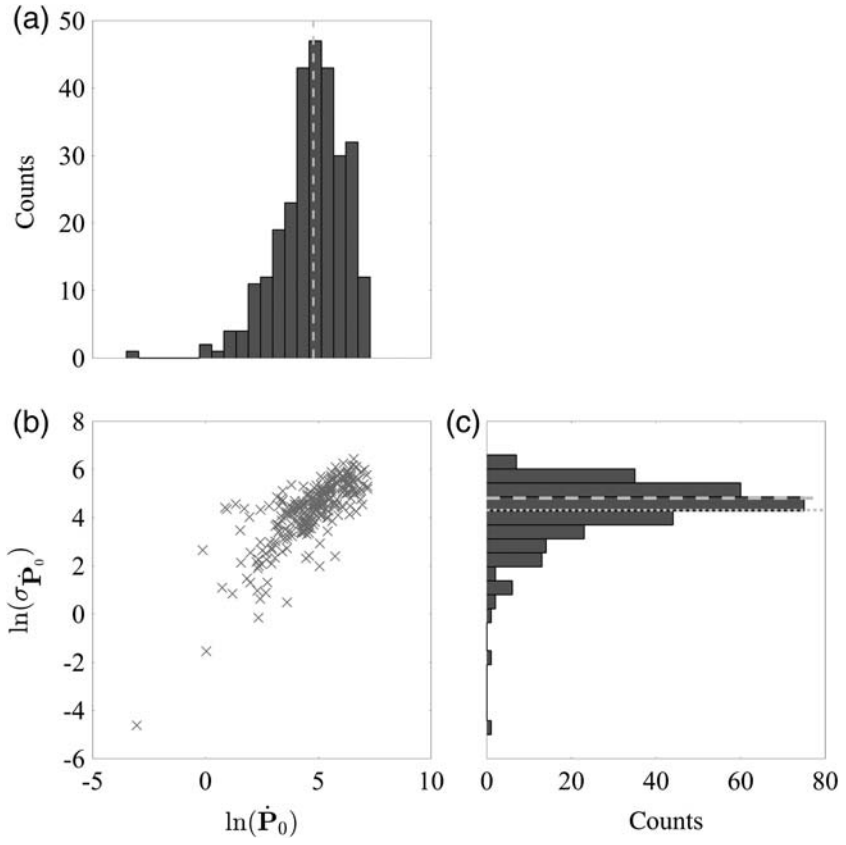

Figure 8. Distributions of mean and standard deviation of potency accumulation rate: (a) histogram of the roughly lognormal distribution of potency accumulation rate per unit depth. 95% of potency (right of vertical dashed line) takes place in 31% of the total area considered, and 52% of the active region; (b) standard deviation of potency accumulation rate is correlated with mean potency accumulation rate; and (c) histogram of standard deviation of potency accumulation rate. The thick horizontal dashed line is the mean standard deviation of $\dot{\mathbf{P}}_0$ (122 $m^3/yr/m$), and the thin horizontal dashed line is log mean of $\dot{\mathbf{P}}_0$ (73 $m^3/yr/m$).

models (Chuang and Johnson, 2011; Johnson, 2013; Tong *et al.*, 2014) (Table 1). Reported uncertainties from studies that consider time-dependent deformation also do not differ significantly from those that assume time-averaged deformation.

Future work may seek alternative metrics as proxies for epistemic uncertainty. For example, rather than calculating a standard deviation on deformation within each grid cell, it may be appropriate to assess uncertainty within each grid cell with a bootstrapping method (Efron, 1979) to reduce the influence of outlier estimates. Another approach might calculate weighted slip rates and standard deviations based on reported uncertainty, an assessment of model quality, or by giving recent studies greater weight.

Results in the Context of UCERF3 Fault Geometry

In many earthquake hazard contexts, estimates of geodetic slip rates on specific faults are desirable for comparison with geologic slip rates and for streamlined integration into a pre-existing decision tree (e.g., Petersen *et al.*, 2014). As a demonstration of how this approach may be directly applicable to earthquake hazard models, I project the SAVGTs onto the UCERF3.1 fault geometry to produce summary strike-slip rates, opening rates, and standard deviations on all UCERF3.1 faults, producing a single summary model of geodetic slip rates in California (Figs. 10, 11). For purposes of this exercise, I only consider UCERF3.1 fault geometries, although it is trivial to extend this analysis to UCERF3.2. Summary slip rates are derived for each UCERF3.1 fault segment by rotating the SAVGT in each grid cell into a fault-parallel orientation for each fault in that grid cell, and converting to slip rate in that orientation following equations (10a–d):

$$\dot{\mathbf{s}}_{\mathbf{k}} = \frac{\bar{v}_{\tilde{y}'\tilde{x}'}\tilde{A}}{\sum_{i=1}^{N}\tilde{L}_i} \tag{13a}$$

$$\dot{\mathbf{t}}_{\mathbf{k}} = \frac{\bar{v}_{\tilde{x}'\tilde{x}'}\tilde{A}}{\sum_{i=1}^{N}\tilde{L}_i} \tag{13b}$$

$$\dot{\mathbf{s}}'_{\mathbf{k}} = \frac{\bar{v}_{\tilde{x}'\tilde{y}'}\tilde{A}}{\sum_{i=1}^{N}\tilde{L}_i} \tag{13c}$$

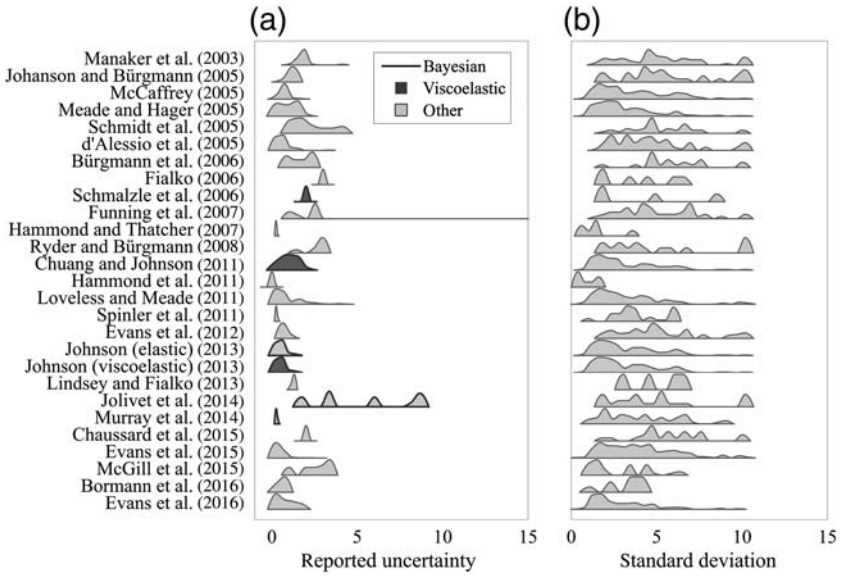

Figure 9. Comparison between reported uncertainties and standard deviation in corresponding grid cells: (a) all reported uncertainties for each study, where available. Distributions represent relative distributions of uncertainty values. Bold outline identifies models that determine uncertainties within a Bayesian approach; darker distributions identify models that calculate slip rates within the model that considers viscoelastic relaxation of the lower crust and/or upper mantle; and (b) standard deviation in corresponding grid cells. Distributions represent relative distributions of standard deviation values.

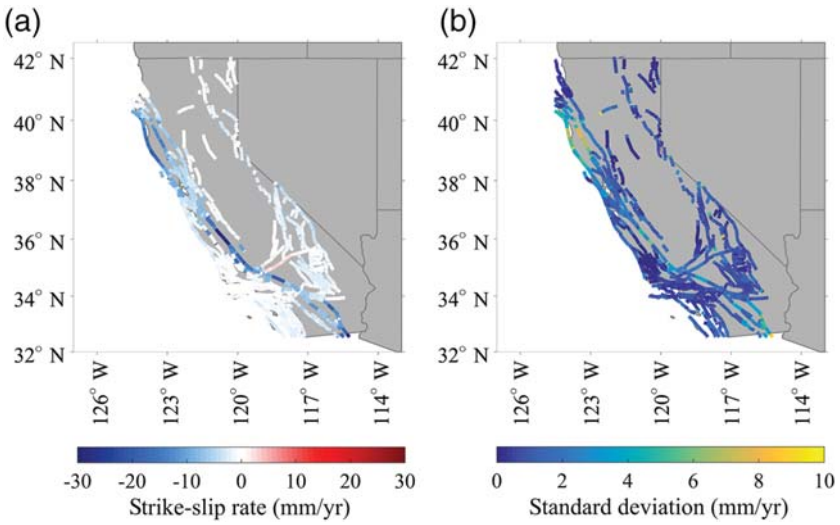

Figure 10. SAVGT over 33 geodetic studies projected into strike-slip rates on the UCERF3.1 fault geometry: (a) mean strike-slip rate and (b) standard deviation of strike-slip rate.

$$\dot{\mathbf{t}}_{\mathbf{k}}^{'} = \frac{\bar{v}_{\tilde{y}'\tilde{y}'}\tilde{A}}{\sum_{i=1}^{N}\tilde{L}_i}, \tag{13d}$$

in which $\tilde{x}'$ and $\tilde{y}'$ are geographic coordinates rotated into the orientation of fault k, $\dot{\mathbf{s}}_{\mathbf{k}}$ and $\dot{\mathbf{t}}_{\mathbf{k}}$ are summary strike-slip and horizontal opening rates on UCERF3.1 fault k, respectively, and $\dot{\mathbf{s}}_{\mathbf{k}}^{'}$ and $\dot{\mathbf{t}}_{\mathbf{k}}^{'}$ are strike-slip and horizontal opening rates on perpendicular structures. N is the number of UCERF3.1 faults contained within the grid cell, and $\tilde{L}_i$ are their arc lengths. Because $\bar{\mathbf{v}}$ represents spatially averaged deformation within each grid cell, equations (13a–d) produce an average slip rate for every fault orientation in the cell. This summary model is an alternative to the UCERF3.1 average block model (ABM) that considers all geodetic slip-rate estimates in California (including the UCERF3.1 ABM).

In general, the summary model strike-slip rates on the San Andreas fault system are higher than ABM rates, and rates on minor faults are slightly lower (Fig. 12 and Ⓔ Table S1). The largest differences occur along the central San Andreas fault, where summary model strike-slip rates on the Carrizo segment are only 17.6 mm/yr, and ABM rates are 28.1 mm/yr. Low summary rates on the Carrizo segment correspond to the presence of multiple faults within a given grid cell because the summary distributes the mean grid cell rate across all faults, not just the main trace. Summary model rates are slightly higher than ABM rates on the creeping segment of the San Andreas fault (27–31 vs. 28.4 mm/yr), and slightly lower than the ABM rates in the central eastern California shear zone, with 2.3 mm/yr on the Calico fault in the summary model, and 5.1 mm/yr in the ABM, again due to the presence of many faults within a single grid cell. Differences in tensile rates between the two models are small, <5 mm/yr. A smaller length-scale grid may be more appropriate for projection onto dense receiver-fault geometries such as the UCERF3.1 faults. However, the length-scale analysis (the Grid Size Assessment section) suggests that smaller grids may be below length-scale characteristic of epistemic uncertainty in fault system geometry based on geodetic observations. In other words, existing deformation models for interpreting geodetic data are currently not sufficient to discriminate between faults at the density and spacing of the UCERF3.1 fault model.

Strike-slip rates perpendicular to UCERF3.1 faults, tensile-slip rates parallel to UCERF3.1 faults, and deformation in grid cells that do not intersect UCERF3.1 faults produce a summary model of OMF deformation (Fig. 13 and Ⓔ Table S2). Fault tips in particular stand out with high OMF deformation, such as at the tips of the Swain Ravine and

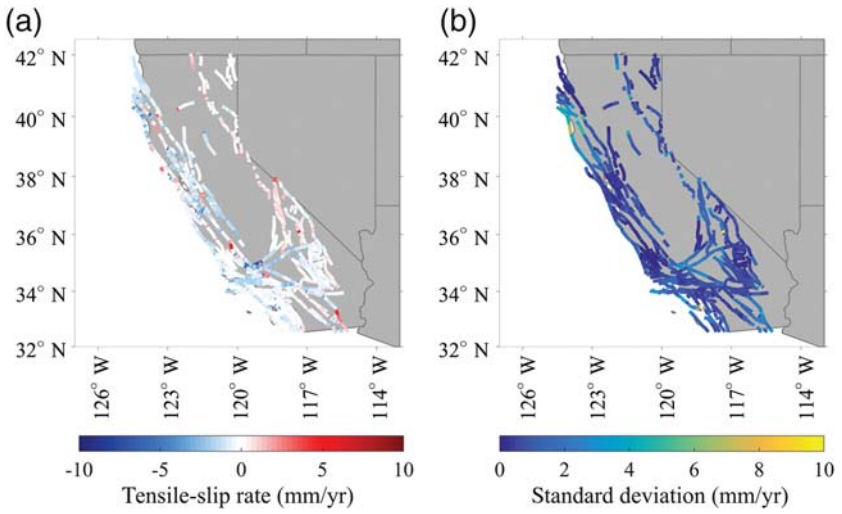

Figure 11. SAVGT statistics over 33 geodetic studies projected into tensile-slip rates on the UCERF3.1 fault geometry: (a) mean tensile-slip rate and (b) standard deviation of tensile-slip rate.

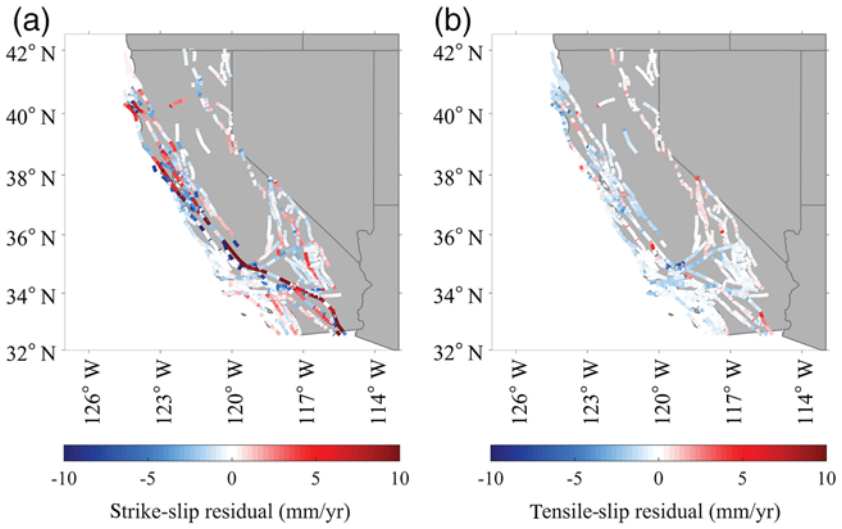

Figure 12. Residual (a) strike slip and (b) tensile deformation between summary deformation from this study projected onto UCERF3.1 faults and the UCERF3.1 average block model.

Battle Creek faults in the northern Central Valley (Fig. 13), highlighting the fact that faults likely do not terminate abruptly, and deformation at fault tips may be distributed (e.g., Herbert *et al.*, 2014) and/or transferred to unmapped structures (e.g., Evans *et al.*, 2012). The magnitude of the SAVGT in each grid cell shows that 28% of the total summary deformation is OMF deformation, which is approximately equal to the 30% UCERF3 estimate of off-fault deformation (Parsons *et al.*, 2013). However, 75% of the total OMF deformation from the summary model occurs in grid cells that intersect with UCERF3.1 faults. Although this result is dependent on grid size, it is clear that most OMF deformation occurs adjacent to UCERF3.1 faults in either the dense or coarse alternate grids (62% and 83%, respectively; Ⓔ Tables S3–S6). OMF deformation may therefore be a by-product of uncertainty in geodetic slip models and may be physically accommodated on, or very near, UCERF faults.

Conclusion

Systematic compilation and analyses of published geodetic slip rates produce a community-averaged deformation model of California, enable holistic comparison with geologic slip rates, and suggest an average model uncertainty of ~1.5 mm/yr. Slip-rate model uncertainties may be much higher near fault junctions and regions of geometric complexity: the largest standard deviation among published geodetic slip-rate estimates is nearly 10 mm/yr—more than twice as large as most reported uncertainties on geodetic slip rate. Accounting for epistemic uncertainty in deformation models, including seismic hazard models, requires incorporating these large, geographically variable uncertainties on geodetic slip rate. Community-averaged potency rates correspond to an $M_w \approx 8.1$ earthquake every 100 yrs. Finally, the summary GSRM resolved onto UCERF3.1 faults suggests that up to 75% of estimated OMF deformation may be physically accommodated on, or very near, UCERF faults, and additional distributed deformation may not be required.

Data and Resources

Calculations, figure generation, and graphical user interface development were done with MATLAB (www.mathworks.com, last accessed May 2017). Maps were created in MATLAB with mapping package M_Map (https://www.eoas.ubc.ca/~rich/map.html, last accessed May 2017). Downloadable files for the Unified California Earthquake Rupture Forecast, v. 3 faults and deformation models are available through the U.S. Geological Survey (USGS) open-file report (https://pubs.usgs.gov/of/2013/1165/, last accessed May 2017). USGS, Arizona Geological Survey, California Geological Survey, Idaho Geological Survey, Nevada Bureau of Mines and Geology, Utah Geological Survey, 2006, and Quaternary fault and fold database for the United States from the USGS website (https://earthquake.usgs.gov/hazards/qfaults/, last accessed May 2017). Advanced National Seismic System catalog data accessed through the Northern California Earthquake Data

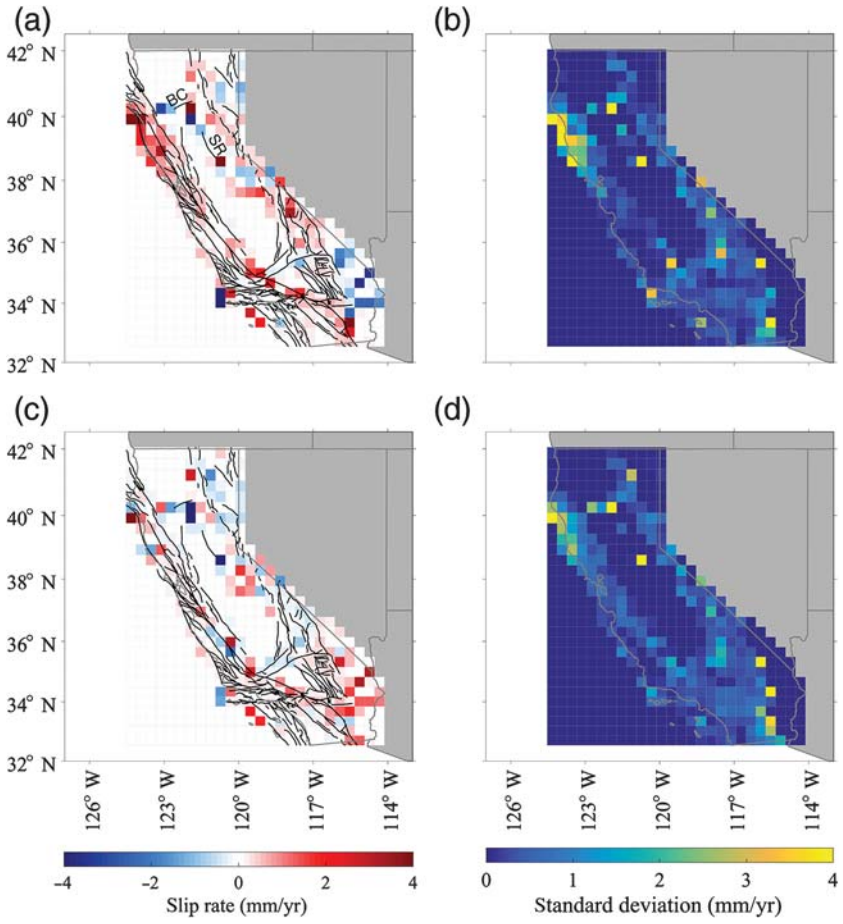

Figure 13. Remaining deformation not projected onto UCERF3.1 fault geometry from summary statistics over 32 geodetic studies: (a) strike-slip rate orthogonal to modeled faults or where no UCERF3.1 faults are present; (b) standard deviation on remaining strike-slip deformation; (c) tensile-slip rate parallel to modeled faults or where no UCERF3.1 faults are present; and (d) standard deviation on remaining tensile deformation. Selected faults labeled: BC, Battle Creek fault; SR, Swain Ravine fault.

Center (doi: 10.7932/NCEDC, last accessed May 2017). Two geodetic slip-rate models were digitized using the GraphClick software (http://www.arizona-software.ch/graphclick/, last accessed May 2017).

Acknowledgments

The author thanks Brendan Meade, Jack Loveless, Sally McGill, Bill Hammond, Jayne Bormann, Elliot Spinler, Kaj Johnson, Ray Chuang, Xiaopeng Tong, and Tom Parsons for providing fault geometries and slip rates from their publications to be included in this analysis; and to all of the authors who included fault geometries and slip rates in their original publication and/or supplementary material (Manaker *et al.*, 2003; Argus *et al.*, 2005; d'Alessio *et al.*, 2005; Johanson and Bürgmann, 2005; McCaffrey, 2005; Schmidt *et al.*, 2005; Bürgmann *et al.*, 2006; Funning *et al.*, 2007; Rolandone *et al.*, 2008; Ryder and Bürgmann, 2008; Bird, 2009; Murray *et al.*, 2014; Chaussard *et al.*, 2015). The author is grateful to Mike Oskin and two anonymous reviewers for thoughtful reviews that greatly improved this article. Thank you to Phoebe DeVries, Andrew Barbour, and Benjamin Brooks for helpful comments on an earlier version of this article, and thank you to Fred Pollitz, Sarah Minson, and Annemarie Sundstrom for many helpful discussions.

References

Argus, D. F., M. B. Heflin, G. Peltzer, F. Crampe, and F. H. Webb (2005). Interseismic strain accumulation and anthropogenic motion in metropolitan Los Angeles, *J. Geophys. Res.* **110,** no. B4, 26, doi: 10.1029/2003jb002934.

Bird, P. (2009). Long-term fault slip rates, distributed deformation rates, and forecast of seismicity in the western United States from joint fitting of community geologic, geodetic, and stress direction data sets, *J. Geophys. Res.* **114,** no. B11, doi: 10.1029/2009jb006317.

Bond, C. E., A. D. Gibbs, Z. K. Shipton, and S. Jones (2007). What do you think this is? "Conceptual uncertainty" in geoscience interpretation, *GSA Today* **17,** no. 11, 4–10, doi: 10.1130/GSAT01711A.1.

Bormann, J. M., W. C. Hammond, C. Kreemer, and G. Blewitt (2016). Accommodation of missing shear strain in the Central Walker Lane, western North America: Constraints from dense GPS measurements, *Earth Planet. Sci. Lett.* **440,** 169–177, doi: 10.1016/j.epsl.2016.01.015.

Budnitz, R. J., G. Apostolakis, D. M. Boore, L. S. Cluff, K. J. Coppersmith, C. A. Cornell, and P. A. Morris (1997). *Recommendations for Probabilistic Seismic Hazard Analysis: Guidance on Uncertainty and Use of Experts, NUREG/CR-6372*, two volumes, U.S. Nuclear Regulatory Commission, Washington, D.C.

Bürgmann, R., G. Hilley, A. Ferretti, and F. Novali (2006). Resolving vertical tectonics in the San Francisco Bay area from permanent scatterer InSAR and GPS analysis, *Geology* **34,** no. 3, 221–224, doi: 10.1130/g22064.1.

Chaussard, E., R. Bürgmann, H. Fattahi, C. W. Johnson, R. Nadeau, T. Taira, and I. Johanson (2015). Interseismic coupling and refined earthquake potential on the Hayward-Calaveras fault zone, *J. Geophys. Res.* **120,** no. 12, 8570–8590, doi: 10.1002/2015jb012230.

Chuang, R. Y., and K. M. Johnson (2011). Reconciling geologic and geodetic model fault slip-rate discrepancies in Southern California: Consideration of nonsteady mantle flow and lower crustal fault creep, *Geology* **39,** no. 7, 627–630, doi: 10.1130/g32120.1.

d'Alessio, M. A., I. A. Johanson, R. Bürgmann, D. A. Schmidt, and M. H. Murray (2005). Slicing up the San Francisco Bay area: Block kinematics and fault slip rates from GPS-derived surface velocities, *J. Geophys. Res.* **110,** no. B6, doi: 10.1029/2004jb003496.

Dawson, T. E., and R. J. Weldon III (2013). Appendix B: Geologic slip rate data and geologic deformation model, *U.S. Geol. Surv. Open-File Rept., 2013-1165-B and California Geol. Surv. Special Rept., 228-B*.

DeMets, C., R. G. Gordon, and D. F. Argus (2010). Geologically current plate motions, *Geophys. J. Int.* **181,** no. 1, 1–80, doi: 10.1111/j.1365-246X.2009.04491.x.

Dixon, T. H., E. Norabuena, and L. Hotaling (2003). Paleoseismology and Global Positioning System: Earthquake-cycle effects and geodetic versus geologic fault slip rates in the eastern California shear zone, *Geology* **31,** no. 1, 55–58, doi: 10.1130/0091-7613(2003)031<0055:pagpse>2.0.co;2.

Douglas, J., and B. Edwards (2016). Recent and future developments in earthquake ground motion estimation, *Earth Sci. Rev.* **160,** 203–219, doi: 10.1016/j.earscirev.2016.07.005.

Efron, B. (1979). Bootstrap methods: Another look at the jackknife, *Ann. Stat.* **7,** no. 1, 1–26, doi: 10.1214/aos/1176344552.

Evans, E. L., J. P. Loveless, and B. J. Meade (2012). Geodetic constraints on San Francisco Bay area fault slip rates and potential seismogenic asperities on the partially creeping Hayward fault, *J. Geophys. Res.* **117,** no. B03410, doi: 10.1029/2011jb008398.

Evans, E. L., J. P. Loveless, and B. J. Meade (2015). Total variation regularization of geodetically and geologically constrained block models for the western United States, *Geophys. J. Int.* **202,** no. 2, 713–727, doi: 10.1093/gji/ggv164.

Evans, E. L., W. R. Thatcher, F. F. Pollitz, and J. R. Murray (2016). Persistent slip rate discrepancies in the eastern California (USA) shear zone, *Geology* **44,** no. 9, 691–694, doi: 10.1130/G37967.1.

Fialko, Y. (2006). Interseismic strain accumulation and the earthquake potential on the southern San Andreas fault system, *Nature* **441,** no. 7096, 968–971, doi: 10.1038/nature04797.

Field, E. H., G. P. Biasi, P. Bird, T. E. Dawson, K. R. Felzer, D. D. Jackson, K. M. Johnson, T. H. Jordan, C. Madden, A. J. Michael, *et al.* (2013). Uniform California Earthquake Rupture Forecast, version 3 (UCERF3)—The time-independent model, *U.S. Geol. Surv. Open-File Rept. 2013–1165*, 97 pp., California Geological Survey Special Report 228, and Southern California Earthquake Center Publication 1792, http://pubs.usgs.gov/of/2013/1165/ (last accessed May 2007).

Funning, G. J., R. Bürgmann, A. Ferretti, and F. Novali (2007). Creep on the Rodgers Creek fault, northern San Francisco Bay area from a 10 year PS-InSAR dataset, *Geophys. Res. Lett.* **34,** no. 19, doi: 10.1029/2007gl030836.

Hammond, W. C., and W. Thatcher (2007). Crustal deformation across the Sierra Nevada, northern Walker Lane, Basin and Range transition, western United States measured with GPS, 2000–2004, *J. Geophys. Res.* **112,** no. B5, doi: 10.1029/2006jb004625.

Hammond, W. C., G. Blewitt, and C. Kreemer (2011). Block modeling of crustal deformation of the northern Walker Lane and Basin and Range from GPS velocities, *J. Geophys. Res.* **116,** no. B4, doi: 10.1029/2010jb007817.

Hearn, E. H., C. T. Onishi, F. F. Pollitz, and W. R. Thatcher (2013). How do "ghost transients" from past earthquakes affect GPS slip rate estimates on southern California faults?, *Geochem. Geophys. Geosys.* **14,** no. 4, 828–838, doi: 10.1002/ggge.20080.

Herbert, J. W., M. L. Cooke, and S. T. Marshall (2014). Influence of fault connectivity on slip rates in southern California: Potential impact on discrepancies between geodetic derived and geologic slip rates, *J. Geophys. Res.* **119,** 2342–2361, doi: 10.1002/2013JB010472.

Johanson, I. A., and R. Bürgmann (2005). Creep and quakes on the northern transition zone of the San Andreas fault from GPS and InSAR data, *Geophys. Res. Lett.* **32,** L14306, doi: 10.1029/2005GL023150.

Johnson, H. O., D. C. Agnew, and K. Hudnut (1994). Extremal bounds on earthquake moment from geodetic data—Application to the Landers earthquake, *Bull. Seismol. Soc. Am.* **84,** no. 3, 660–667.

Johnson, K. M. (2013). Slip rates and off-fault deformation in Southern California inferred from GPS data and models, *J. Geophys. Res.* **118,** no. 10, 5643–5664, doi: 10.1002/jgrb.50365.

Jolivet, R., M. Simons, P. S. Agram, Z. Duputel, and Z. K. Shen (2015). Aseismic slip and seismogenic coupling along the central San Andreas fault, *Geophys. Res. Lett.* **42,** no. 2, 297–306, doi: 10.1002/2014gl062222.

Lindsey, E. O., and Y. Fialko (2013). Geodetic slip rates in the southern San Andreas fault system: Effects of elastic heterogeneity and fault geometry, *J. Geophys. Res.* **118,** no. 2, 689–697, doi: 10.1029/2012jb009358.

Loveless, J. P., and B. J. Meade (2011). Stress modulation on the San Andreas fault by interseismic fault system interactions, *Geology* **39,** no. 11, 1035–1038, doi: 10.1130/g32215.1.

Mai, P. M., and K. K. S. Thingbaijam (2014). SRCMOD: An online database of finite-fault rupture models, *Seismol. Res. Lett.* **85,** no. 6, 1348–1357, doi: 10.1785/0220140077.

Manaker, D. M., R. Bürgmann, W. H. Prescott, and J. Langbein (2003). Distribution of interseismic slip rates and the potential for significant earthquakes on the Calaveras fault, central California, *J. Geophys. Res.* **108,** no. B6, doi: 10.1029/2002jb001749.

Maurer, J., and K. Johnson (2014). Fault coupling and potential for earthquakes on the creeping section of the central San Andreas fault, *J. Geophys. Res.* **119,** 4414–4428, doi: 10.1002/2013JB010741.

Maurer, J., P. Segall, and A. M. Bradley (2017). Bounding the moment deficit rate on crustal faults using geodetic data: Methods, *J. Geophys. Res.* **122,** 6811–6835, doi: 10.1002/2017JB014300.

McCaffrey, R. (2005). Block kinematics of the Pacific–North America plate boundary in the southwestern United States from inversion of GPS, seismological, and geologic data, *J. Geophys. Res.* **110,** no. B7, doi: 10.1029/2004jb003307.

McGill, S. F., J. C. Spinler, J. D. McGill, R. A. Bennett, M. A. Floyd, J. E. Fryxell, and G. J. Funning (2015). Kinematic modeling of fault slip rates using new geodetic velocities from a transect across the Pacific–North America plate boundary through the San Bernardino Mountains, California, *J. Geophys. Res.* **120,** no. 4, 2772–2793, doi: 10.1002/2014jb011459.

Meade, B. J. (2007). Power-law distribution of fault slip-rates in southern California, *Geophys. Res. Lett.* **34,** no. 23, doi: 10.1029/2007gl031454.

Meade, B. J., and B. H. Hager (2005). Block models of crustal motion in southern California constrained by GPS measurements, *J. Geophys. Res.* **110,** no. B03403, doi: 10.1029/2004jb003209.

Meade, B. J., Y. Klinger, and E. A. Hetland (2013). Inference of multiple earthquake-cycle relaxation timescales from irregular geodetic sampling of interseismic deformation, *Bull. Seismol. Soc. Am.* **103,** no. 5, 2824–2835, doi: 10.1785/0120130006.

Murray, J. R., S. E. Minson, and J. L. Svarc (2014). Slip rates and spatially variable creep on faults of the northern San Andreas system inferred through Bayesian inversion of Global Positioning System data, *J. Geophys. Res.* **119,** no. 7, 6023–6047, doi: 10.1002/2014jb010966.

Nicol, A., R. J. Van Dissen, M. W. Stirling, and M. C. Gerstenberger (2016). Completeness of the paleoseismic active-fault record in New Zealand, *Seismol. Res. Lett.* **87,** no. 6, 1299–1310, doi: 10.1785/0220160088.

Okada, Y. (1985). Surface deformation due to shear and tensile faults in a half-space, *Bull. Seismol. Soc. Am.* **75,** no. 4, 1135–1154.

Parsons, T., K. M. Johnson, P. Bird, J. Bormann, T. E. Dawson, E. H. Field, W. C. Hammond, T. A. Herring, R. McCaffrey, Z.-K. Shen, *et al.* (2013). Appendix C: Deformation models for UCERF3, *U.S. Geol. Surv. Open-File Rept. 2013–1165*, 97 pp., California Geological Survey Special Report 228, and Southern California Earthquake Center Publication 1792, http://pubs.usgs.gov/of/2013/1165/ (last accessed May 2007).

Petersen, M. D., M. P. Moschetti, P. M. Powers, C. S. Mueller, K. M. Haller, A. D. Frankel, Y. Zeng, S. Rezaeian, S. C. Harmsen, O. S. Boyd, *et al.* (2014). Documentation for the 2014 update of the United States national seismic hazard maps, *U.S. Geol. Surv. Open-File Rept. 2014-1091*, 243 pp., doi: 10.3133/ofr20141091.

Rolandone, F., R. Bürgmann, D. C. Agnew, I. A. Johanson, D. C. Templeton, M. A. d'Alessio, S. J. Titus, C. DeMets, and B. Tikoff (2008). Aseismic slip and fault-normal strain along the central creeping section of the San Andreas fault, *Geophys. Res. Lett.* **35,** no. 14, doi: 10.1029/2008gl034437.

Ryder, I., and R. Bürgmann (2008). Spatial variations in slip deficit on the central San Andreas fault from InSAR, *Geophys. J. Int.* **175,** no. 3, 837–852, doi: 10.1111/j.1365-246X.2008.03938.x.

Sauber, J., W. Thatcher, S. C. Solomon, and M. Lisowski (1994). Geodetic slip rate for the eastern California shear zone and the recurrence time of Mojave Desert earthquakes, *Nature* **367,** no. 6460, 264–266, doi: 10.1038/367264a0.

Savage, J. C., and R. O. Burford (1973). Geodetic determination of relative plate motion in central California, *J. Geophys. Res.* **78,** no. 5, 832–845.

Savage, J. C., and R. W. Simpson (2013). Clustering of velocities in a GPS network spanning the Sierra Nevada Block, the northern Walker Lane Belt, and the central Nevada Seismic Belt, California-Nevada, *J. Geophys. Res.* **118,** 4937–4947, doi: 10.1002/jgrb.50340.

Schmalzle, G., T. Dixon, R. Malservisi, and R. Govers (2006). Strain accumulation across the Carrizo segment of the San Andreas fault,

California: Impact of laterally varying crustal properties, *J. Geophys. Res.* **111,** no. B5, doi: 10.1029/2005jb003843.

Schmidt, D. A., R. Bürgmann, R. M. Nadeau, and M. d'Alessio (2005). Distribution of aseismic slip rate on the Hayward fault inferred from seismic and geodetic data, *J. Geophys. Res.* **110,** no. B8, doi: 10.1029/2004jb003397.

Segall, P. (2010). *Earthquake and Volcano Deformation*, Princeton University Press, Princeton, New Jersey, 432 pp.

Smith-Konter, B. R., D. T. Sandwell, and P. Shearer (2011). Locking depths estimated from geodesy and seismology along the San Andreas Fault System: Implications for seismic moment release, *J. Geophys. Res.* **116,** no. B06401, doi: 10.1029/2010JB008117.

Spinler, J. C., R. A. Bennett, M. L. Anderson, S. F. McGill, S. Hreinsdottir, and A. McCallister (2010). Present-day strain accumulation and slip rates associated with southern San Andreas and eastern California shear zone faults, *J. Geophys. Res.* **115,** no. B11, doi: 10.1029/2010jb007424.

Thatcher, W., J. C. Savage, and R. W. Simpson (2016). The eastern California shear zone as the northward extension of the southern San Andreas fault, *J. Geophys. Res.* **121,** no. 4, 2904–2914, doi: 10.1002/2015jb012678.

Tong, X., B. Smith-Konter, and D. T. Sandwell (2014). Is there a discrepancy between geological and geodetic slip rates along the San Andreas Fault System?, *J. Geophys. Res.* **119,** no. 3, 2518–2538, doi: 10.1002/2013jb010765.

York, D., N. M. Evensen, M. L. Martinez, and J. D. Delgado (2004). Unified equations for the slope, intercept, and standard errors of the best straight line, *Am. J. Phys.* **72,** no. 3, 367–375, doi: 10.1119/1.1632486.

Zeng, Y., and Z.-K. Shen (2014). Fault network modeling of crustal deformation in California constrained using GPS and geologic observations, *Tectonophysics* **612/613,** 1–17.

Zeng, Y. H., and Z.-K. Shen (2016). A fault-based model for crustal deformation, fault slip rates, and off-fault strain rate in California, *Bull. Seismol. Soc. Am.* **106,** no. 2, 766–784, doi: 10.1785/0120140250.

U.S. Geological Survey
345 Middlefield Road, MS 977
Menlo Park, California 94025
elevans11@gmail.com

Manuscript received 31 May 2017;
Published Online 14 November 2017